

Doppler-free spectroscopy of the lowest triplet states of helium using double optical resonance

Ali Dia^{1,2}, Marie Abboud², Pierre-Jean Nacher^{*1}, and Geneviève Tastevin¹

¹*Laboratoire Kastler Brossel, ENS-Université PSL, CNRS, Sorbonne Université, Collège de France; 24 rue Lhomond, 75005 Paris, France.*

²*Physics Department, UR TVA, Faculty of Science, Saint Joseph University, BP 11-514 Riad El Solh, Beirut 11072050, Lebanon*

Abstract Optical pumping on the 2^3S – 2^3P transition (1083 nm) of metastable ^3He or ^4He atoms is used for fundamental science and applications. We report on its combination with an optical probe on the 2^3P – 3^3S transition (706.5 nm) in a ladder-type double optical resonance scheme, with CW single-frequency pump and probe diode lasers. Theoretical expectations for level structure and absorption spectra were computed for both isotopes. Narrow Doppler-free absorption lines were experimentally obtained in low-pressure gas samples. The line weights and Zeeman structure in weak magnetic field agreed with expectations. The precision of the line positions and line splittings was limited by generic errors of our commercial Fizeau wavemeter, which were independently characterised. The potential of this double resonance scheme for spectroscopic measurements on the three lowest triplet states of He was evaluated. The relevance of velocity- and sublevel-selective pumping combined with polarisation spectroscopy of probe absorption for a study of pressure-dependent population transfers in the 2^3P state was established.

1 Introduction

The two lowest-lying triplet electronic states of helium are involved in the 1083 nm optical transition used to perform optical pumping (OP) of the 2^3S metastable state, which is usually populated by a radiofrequency (RF) discharge in a low-pressure gas. In ^3He , OP is the driving term of metastability-exchange optical pumping (MEOP), an efficient process yielding high nuclear polarisations in the atomic ground state and used in many applications, ranging from fundamental physics to medical imaging [1]. Additional features resulting from polarisation in the 2^3S state are also investigated in gas discharges in ^3He [2, 3, 4] or used in ^4He for a variety of magnetometer schemes [5, 6, 7]. One important physical process affecting the operation and efficiency of the 2^3S – 2^3P OP cycle is the redistribution of atoms among sublevels of the 2^3P state during the radiative lifetime as a result of collisions with ground-state atoms of the gas. Its pressure-dependent influence may be strong, yielding for instance a change in the sign of the OP-induced polarisation between low and high gas pressure [1, Sect. III.C.2].

In spite of the importance of 1^1S – 2^3P collisions, detailed studies of collisional rates in RF gas discharges (as well as quantitative analysis of their contribution to OP dynamics for both isotopes) are still missing. Only few theoretical evaluations [8, 9] and one global indirect measurement [10] of the cross-sections for collisional transfer between ^4He fine structure levels were reported. We therefore designed an experiment to measure collisional transfer rates within the 2^3P manifold for both isotopes and to establish correlations with OP dynamics features. Gaseous He

samples were submitted to velocity-selective OP (VSOP) on the 2^3S – 2^3P transition at 1083 nm and steady-state distributions of atomic populations and velocities in the 2^3P state were probed by laser absorption on the 2^3P – 3^3S transition at 706.5 nm. A (co-propagating) collinear pump-probe configuration was chosen to maximise probe light absorption and to avoid residual Doppler broadenings at 706.5 nm (potentially large, compared to the natural widths, in He). Combination of absorption spectroscopy and polarimetry at 706.5 nm allowed quantitative assessment of atomic number densities in the probed 2^3P sublevels, as well as discrimination between atoms selectively excited by the pump laser and atoms transferred to other velocity classes or sublevels by collisions.

Initial evidence of population transfers due to 1^1S – 2^3P collisions was very briefly reported for isotopic mixtures [11]. The results of a detailed study of collisional transfer rates between fine or hyperfine 2^3P sublevels will be reported in a forthcoming article. Here, we mainly focus on the 2^3S – 2^3P – 3^3S three-level ladder system involved in the measurements and on the analysis of double optical resonance signals obtained when the effect of collisions is weak. We report on expected and measured Doppler-free spectroscopic data for the 2^3P – 3^3S transition at 706.5 nm in ^3He and ^4He . We also provide an example of 706.5 nm absorption spectrum obtained by double optical resonance when strong collisional mixing occurs. The advantageous boost in signal amplitude associated with the use of 1083 nm pumping may be appreciated by comparison with prior Doppler-limited spectroscopic investigations at 706.5 nm in He gas cells and RF glow discharges, with techniques such as analysis of fluorescence spectra (yielding hyperfine splittings of ^3He levels and isotope shifts [12, 13], or pressure broadening [14] and pres-

*nacher@lkb.ens.fr, corresponding author.

sure shift [15] in ^4He) and optogalvanic detection of laser absorption at 706.5 nm [16] (yielding 3^3S hyperfine splittings, with a data fitting accuracy that was comparable to that of Doppler-free saturated absorption measurements).

The present article is organised as follows. Section 2 describes the computed fine, hyperfine, and Zeeman components of the 2^3P – 3^3S transition. Absorbance data at 706.5 nm and at 1083 nm are quantitatively linked with atomic number densities in the 2^3P magnetic sublevels and spectral features of the double optical resonance signals are discussed. Section 3 describes the experimental setup and the main elements used for the measurements. The latter include a commercial wavemeter, whose behaviour and stability are characterised in Appendix A. Section 4 compiles experimental results obtained with pure or mixed helium isotopes, at various gas pressures in the millibar range. Typical double optical spectra are presented, together with recordings made at moderately higher pressure (up to 67 mbar) that illustrate the observed changes in line shapes. Zeeman-split spectra at 706.5 nm are compared with expectations at a few milliteslas and the influence of pump intensity on probe absorption signals is reported. Then, the potential of the method and of the experimental arrangement for Doppler-free spectroscopy is evaluated. Compiled low-pressure data sets are used for measurements of the hyperfine structure of the 3^3S state and of the isotope shift of the 2^3P – 3^3S transition. Finally, Section 5 provides a discussion of the current limits and assets of double optical resonance of metastable helium.

2 Theory

2.1 Atomic structures and optical transitions

The fine and hyperfine structures of the three lowest triplet states of helium involved in the 2^3S – 2^3P – 3^3S double optical resonance scheme are schematically depicted in Fig. 1 for both helium isotopes. The structures of the 2^3S and 2^3P states give rise to the various energy shifts (listed in Table 1) for the sublevels of given J -values (for ^4He) or F -values (for ^3He) involved in the 1083 nm optical transition. The remaining degeneracies between magnetic sublevels are removed when a magnetic field is applied and the Zeeman effect becomes significant. The sublevel naming conventions depicted in Fig. 1, the magnetic-field-dependence of the sublevel energies, and the positions and weights of the optical transitions components can be found in Ref. [17]. The null-field positions are reproduced in Table 2 for convenience.

Using the same approach, the level structure of the 3^3S state was computed in the decoupled representations (L, S for ^4He or L, S, I for ^3He). It is indeed similar to that of the metastable 2^3S state and differs mostly because of the $\sim 3\%$ lower value of its hyperfine structure constant

[18, Table 7]:

$$A_S(2^3S) = 4493.13 \text{ MHz}, \quad A_S(3^3S) = 4372.89 \text{ MHz}. \quad (1)$$

We therefore systematically use similar notations for all quantities related to these two states, with a star added as left upper index to denote those pertaining to atomic sublevels of the 3^3S state (such as the sublevel names in Fig. 1) or to 706.5 nm line components.

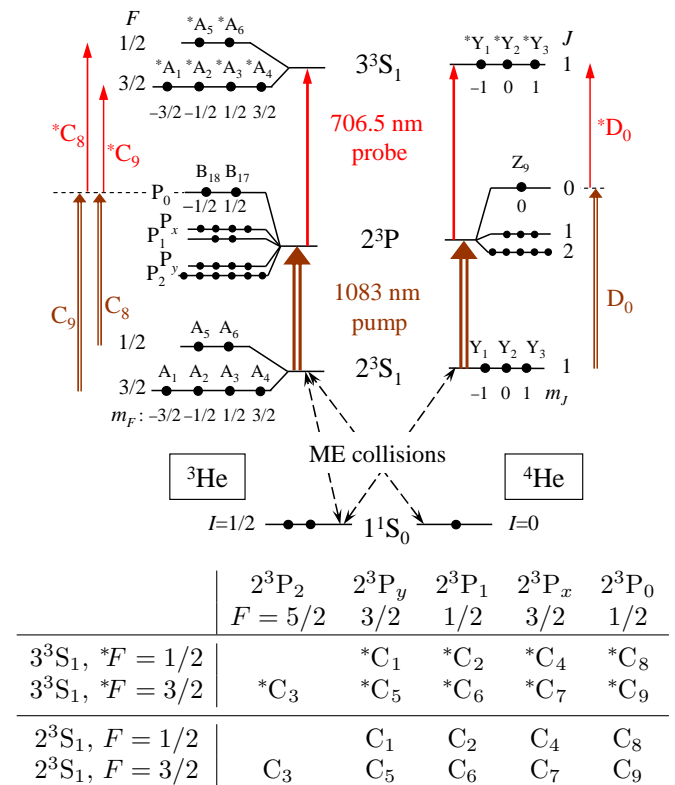


Figure 1: Ground state and lowest triplet states of ^3He (left) and ^4He (right) in null magnetic field. Level spacings and energy splittings associated with J - or F -values of the electronic or total angular momenta are not displayed to scale. Bullets represent Zeeman sublevels; for clarity, names (B or Z labels, with energy-ordered subscripts) are omitted in the 2^3P state except for the highest-lying ones [17]). Actually pump and probe transitions (arrows) only address one or a few magnetic sublevels, selected by choice of light beam polarisation and frequency. Commonly used line components are displayed next to the level diagram. Line components names for pump and probe transitions in ^3He are tabulated (Column headers: names and F -values of the 2^3P levels. Lines: hyperfine 3^3S levels). Line components D_J and $*D_J$ involve the 2^3P_J level in ^4He ($J = 0$ to 2). Metastability-exchange (ME) collisions, displayed for completeness, play no role in optical transitions.

The upper part of Table 1 lists the null-field ^3He energy terms (in units of frequency) of the various hyperfine levels computed using the effective Hamiltonian of Ref. [17]. The computed low-field variations of the en-

^3He level	$\hat{E}(0)/h$ (GHz)	\hat{g}_F -factor
$3^3S, F=1/2$	4.37289	2.66888
$3^3S, F=3/2$	-2.18645	1.3356
$2^3P_0, F=1/2$	32.23217	-0.17635
$2^3P_x, F=3/2$	4.80841	1.41962
$2^3P_1, F=1/2$	4.13924	2.1795
$2^3P_y, F=3/2$	-0.37235	1.38262
$2^3P_2, F=5/2$	-2.15305	1.20129
$2^3S, F=1/2$	4.49313	2.66888
$2^3S, F=3/2$	-2.24657	1.3356
^4He level	$E_P^{(4)}(0)/h$ (GHz)	g_J -factor
$2^3P_0, J=0$	31.90812	
$2^3P_1, J=1$	2.29118	1.50106
$2^3P_2, J=2$	0	1.50106

Table 1: List of computed He level energy terms at $B = 0$: ${}^*E_S/h$, E_P/h , and E_S/h for ^3He (upper part), and $E_P^{(4)}/h$ for ^4He (lower part). The third column lists the \hat{g}_F - and g_J -factors involved in the linear Zeeman energy shifts for these levels.

ergy terms with magnetic field strength B for all Zeeman sublevels were used to extract the linear coefficients, expressed for each of the nine ^3He levels listed in Table 1 as

$$\hat{E}(B) - \hat{E}(0) = \hat{g}_F \hat{m}_F \mu_B B + \mathcal{O}(B^2) \quad (2)$$

where μ_B is the Bohr magneton, \hat{E} , \hat{g}_F , and \hat{m}_F are generic notations for the energy, Landé factor, and angular momentum projection of a sublevel. We more generally use hat-decorated symbols for all quantities and names that may consistently pertain to the ^3He or ^4He isotope, as well as to the 706.5 or 1083 nm transition, in text or equations.

The lower part of Table 1 lists the null-field energy terms of the three 2^3P_J levels of ^4He . Their low-field linear variations are

$$E_P^{(4)}(B) - E_P^{(4)}(0) = g_J m_J \mu_B B + \mathcal{O}(B^2) \quad (3)$$

with g_J given in Table 1. The low-field linear variations for the 3^3S and 2^3S states are simply given by the linear Zeeman energy terms

$${}^*E_S^{(4)}(B) = {}^*g_S {}^*m_S \mu_B B, \quad E_S^{(4)}(B) = g_S m_S \mu_B B, \quad (4)$$

where ${}^*g_S \approx g_S = 2.00224$ [19, Table 5].

The effective Hamiltonian of Ref. [17] yields accurate energy differences only between sublevels of each of the three states considered here. Absolute optical transition energies cannot be inferred. However, energy or frequency differences between optical transitions can be computed from the level energies of Table 1. The results are displayed in Table 2 as a list of computed null-field frequency offsets (or frequencies, for compactness) ${}^*\hat{\varepsilon}/h$ (resp. $\hat{\varepsilon}/h$) from the highest- (resp. lowest-) energy component of the

706.5 nm (resp. 1083 nm) transition, for both isotopes. The energy differences ${}^*\hat{\varepsilon}$ and $\hat{\varepsilon}$ are usually displayed with one index (that of the line component) for null-field situations or with two indices (those of the relevant sublevels) in applied fields.

706.5 nm transition		1083 nm transition	
line	${}^*\hat{\varepsilon}_n/h$ (GHz)	line	$\hat{\varepsilon}_n/h$ (GHz)
*C_1	0	C_1	0
*C_2	-4.51159	C_2	4.51159
*C_3	-4.77864	C_3	4.959
*C_4	-5.18076	C_4	5.18076
*C_5	-6.55934	C_5	6.7397
*C_6	-11.07093	C_6	11.25129
*C_7	-11.7401	C_7	11.92046
*C_8	-32.60452	C_8	32.60452
*C_9	-39.16386	C_9	39.34422
line	${}^*\varepsilon_n^{(4)}/h$ (GHz)	line	$\varepsilon_n^{(4)}/h$ (GHz)
*D_2	-5.33963	D_2	38.53362
*D_1	-7.6308	D_1	40.82479
*D_0	-37.24775	D_0	70.44174

Table 2: List of computed ^3He and ^4He frequencies (i.e. frequency offsets from *C_1 and C_1) of all line components at $B = 0$. These values are used in Fig. 2

For ^3He they are written as

$$\begin{aligned} {}^*\varepsilon_{jk} &= [{}^*E_S({}^*A_k) - {}^*E_S({}^*A_5)] - [E_P(B_j) - E_P(B_7)] \\ \varepsilon_{ij} &= [E_P(B_j) - E_P(B_7)] - [E_S(A_i) - E_S(A_5)]. \end{aligned} \quad (5)$$

The frequencies of *C_n and C_n are exactly opposite when they involve the same $F = 1/2$ hyperfine level as *C_1 and C_1 , namely for $n = 2, 4$, and 8 (see the table in Fig. 1).

For ^4He the null-field line splittings solely result from the fine-structure of the 2^3P level. The line positions with respect to the 706.5 nm ^3He lines are computed using the average of the two published values of isotope shift differences ΔE between level energies of ^4He and ^3He , namely

$${}^*\delta_{\text{iso.}} = \Delta E/h(3^3S_1) - \Delta E/h(2^3P_0) = 594.106 \text{ MHz} \quad (6)$$

according to [20, Table 2] and

$${}^*\delta_{\text{iso.}} = 594.658 \text{ MHz} \quad (7)$$

according to [18, Table 1]. The computation of line positions listed in Table 2 for the *D_n components involves this difference in energy terms, and

$$\begin{aligned} {}^*\varepsilon_{jk}^{(4)} &= [{}^*E_S^{(4)}({}^*Y_k) - {}^*E_S({}^*A_5)] \\ &\quad - [E_P^{(4)}(Z_j) - E_P(B_7)] - {}^*\delta_{\text{iso.}} \end{aligned} \quad (8)$$

where the $B_7-{}^*A_5$ transition of ^3He (*C_1 component) at $B = 0$ is used as a reference for all frequency offsets. The

values in Eqs. 6 and 7 differ by an amount (0.55 MHz) which can safely be neglected in this work but may be experimentally settled rather easily.

Note that the ≈ 0.6 GHz isotope shift is smaller than Doppler widths at room temperature (listed in Table 3). This results in fully overlapping Doppler-broadened spectra for the 706.5 nm lines (Fig. 2c and [12, 13]), a feature which contrasts with the 32 GHz isotope shift for the 1083 nm lines (Fig. 2d).

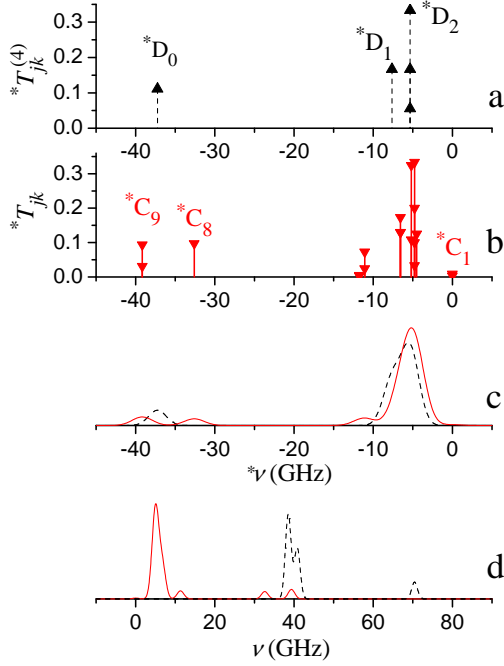


Figure 2: Computed transition matrix elements ${}^*T_{jk}$ (a: ^4He , b: ^3He) and Doppler spectra at 300 K (c: both isotopes) for the 706.5 nm transition at $B = 0$. d: Doppler spectra for the 1083 nm transition. ${}^*T_{jk}$ data (a, b) are displayed for circular polarisation (Tables 5 and 4). Symbols or drop lines overlap for degenerate Zeeman components. Names are indicated for the lines of special interest. Line component positions (frequency offsets ${}^*\hat{\varepsilon}_n/h$) are all referenced to *C_1 . c, d: The scaled spectral functions $\hat{\Delta}\sqrt{\pi}\hat{S}_{\text{th}}$ (Eq. 21; dotted lines: ^4He , solid lines: ^3He) display mirrored features, however with a much larger isotope shift (note the twice larger horizontal scale in d) and better-resolved components (Doppler widths are smaller) at 1083 nm.

Transition matrix elements ${}^*T_{jk}(e_\lambda)$ for ^3He between sublevels B_j and *A_k and ${}^*T_{jk}^{(4)}(e_\lambda)$ for ^4He between sublevels Z_j and *Y_k are computed for the three light polarisation states e_λ (σ_+ , σ_- , and π). Their values at null field are listed in Tables 4 and 5 and displayed in Figs. 2a and 2b. The empty cells correspond to null values of ${}^*T_{jk}$ (forbidden dipolar electric transitions, $|\Delta F| > 1$ or $|\Delta m_F| > 1$ for ^3He , $|\Delta \hat{m}| > 1$ for ^4He).

For both optical transitions the matrix elements correspond to branching ratios for radiative decay and obey similar sum rules. For instance, partial sums over the

	^3He	^4He
1083 nm	$\Delta_3 = 1.1875$	$\Delta_4 = 1.0284$
706.5 nm	${}^*\Delta_3 = 1.8203$	${}^*\Delta_4 = 1.5764$

Table 3: Values of the Doppler width parameters (generically noted $\hat{\Delta}$) in GHz, for ^3He and ^4He and for both optical transitions. They are computed for a temperature $T = 300$ K as $\hat{\Delta} = \hat{\nu}\sqrt{2k_B T/\hat{M}c^2}$ ($\hat{\nu}$ is the optical transition frequency, k_B the Boltzmann constant, and \hat{M} the atomic mass). The Doppler FWHM values are $2\hat{\Delta}\sqrt{\ln 2}$.

	*A_1	*A_2	*A_3	*A_4	*A_5	*A_6
B_1	1/3					
B_2	2/15	1/5				
B_3	1/30	1/5	1/10			
B_4		1/10	1/5	1/30		
B_5			1/5	2/15		
B_6				1/3		
B_7	.19465	.12977			.00891	
B_8	.12977	.02163	.17302		.00594	.00297
B_9		.17302	.02163	.12977	.00297	.00594
B_{10}			.12977	.19465		.00891
B_{11}	.07296	.04864	.02432		.06247	.12494
B_{12}		.02432	.04864	.07296	.12494	.06247
B_{13}	.00535	.00357			.32442	
B_{14}	.00357	.00059	.00475		.21628	.10814
B_{15}		.00475	.00059	.00357	.10814	.21628
B_{16}			.00357	.00535		.32442
B_{17}		.031232	.06247	.09370	.09728	.04864
B_{18}	.09370	.06247	.03123		.04864	.09728

Table 4: ^3He transition matrix elements ${}^*T_{jk}$ between sublevels B_j and *A_k for $B = 0$. The color (online) indicates the light polarisation vector: red for σ_+ , black for π , and blue for σ_- . It corresponds to the angular momentum change between the half-integer \hat{m} -values (m_F and *m_F , not displayed in this table).

lower sublevels for each upper sublevel in the 3^3S state verify

$$\sum_{j,e_\lambda} {}^*T_{jk}^{(4)}(e_\lambda) = \sum_{j,e_\lambda} {}^*T_{jk}(e_\lambda) = 1. \quad (9)$$

Additionally, the ^4He matrix elements of the two transitions verify exact relations:

$${}^*T_{jk}^{(4)}(\sigma_\pm) = T_{kj}^{(4)}(\sigma_\mp)/3, \quad {}^*T_{jk}^{(4)}(\pi) = T_{kj}^{(4)}(\pi)/3, \quad (10)$$

where the opposite helicities of light result from the opposite roles (upper or lower level) of the 3^3S and 2^3S states in the optical transitions. The ^3He matrix elements verify similar relations only for $B = 0$, with small differences (for instance of order 10^{-3} at $B = 0.1$ T) resulting from the difference in hyperfine structure constant values (Eq. 1):

$${}^*T_{jk}(\sigma_\pm) \approx T_{kj}(\sigma_\mp)/3, \quad {}^*T_{jk}(\pi) \approx T_{kj}(\pi)/3. \quad (11)$$

	\hat{m}	*Y_1	*Y_2	*Y_3
		-1	0	1
Z_1	-2	1/3		
Z_2	-1	1/6	1/6	
Z_3	0	1/18	2/9	1/18
Z_4	1		1/6	1/6
Z_5	2			1/3
Z_6	-1	1/6	1/6	
Z_7	0	1/6	0	1/6
Z_8	1		1/6	1/6
Z_9	0	1/9	1/9	1/9

Table 5: ^4He transition matrix elements $^*T_{jk}^{(4)}$ between sublevels Z_j and *Y_k for $B = 0$. The color (online) indicates the light polarisation vector: red for σ_+ , black for π , and blue for σ_- . It corresponds to the angular momentum change between the \hat{m} -values m_j and *m_S .

2.2 Probe transmittance

Explicit expressions for the transmittance \mathcal{T} of a weak probe beam through a helium gas sample can be written when several simplifying assumptions are made: the probe light has one of the three polarisation states e_λ , the probe beam has a small transverse size (across which the populations of all states are uniform), and the probe intensity is weak enough for stimulated emission to be negligible. In this article the probe beam is tuned to the 706.5 nm transition but most results in this section apply for a weak probe on the 1083 nm transition as well. In addition to the hat-decorated notations introduced in Sect. 2.1, we therefore use complementary generic notations for the lower (L) and higher (H) states of a transition in an isotope, with degeneracies g_L and g_H , sublevels L_p and H_q , and populations l_p in the lower state. Note that l_p are true populations (with $\sum a_i = \sum y_i = 1$) only for the 2^3S state. The (pseudo)populations b_j , z_j , *a_k , and *y_k are convenient parameters to obtain the number densities of the corresponding 2^3P state sublevels from \hat{n} , as detailed in Table 6, where the local metastable number density \hat{n} stands for the isotope-specific notations n_m or $n_m^{(4)}$ of Ref. [17].

The probe light intensity $I_{\text{pr.}}$ decreases with z , the position along the light path, when propagating in the sample because of absorbed and scattered light

$$-\frac{dI_{\text{pr.}}}{dz} = h\nu_{\text{pr.}}\hat{n} \sum_{p,q} l_p \int dv_z \phi_{Lp}(v_z) \hat{\gamma}_{pq}(v_z), \quad (12)$$

in which $\nu_{\text{pr.}}$ is the central probe laser frequency, ϕ_{Lp} is the normalised velocity distribution in sublevel L_p , and $\hat{\gamma}_{pq}$ is the velocity-dependent optical transition rate from L_p to H_q . For a normalised frequency distribution $\mathcal{F}(\nu - \nu_{\text{pr.}})$ of the probe light intensity, the transition rates may be

atom	state	sublevel	pop.	density m^{-3}	vel. distr. $(\text{m/s})^{-1}$
^3He	3^3S	*A_k	*a_k	$n_m^*a_k$	
^3He	2^3P	B_j	b_j	$n_m b_j$	$\phi'_j(v_z)$
^3He	2^3S	A_i	a_i	$n_m a_i$	$\phi_i(v_z)$
^4He	3^3S	*Y_k	*y_k	$n_m^{(4)}^*y_k$	
^4He	2^3P	Z_j	z_j	$n_m^{(4)} z_j$	$\phi_j^{(4)}(v_z)$
^4He	2^3S	Y_i	y_i	$n_m^{(4)} y_i$	$\phi_i^{(4)}(v_z)$

Table 6: List of notations used to characterise local quantities for both He isotopes in the relevant states and sublevels (first three columns). The (true) populations in the 2^3S state verify $\sum a_i = \sum y_i = 1$, while the (pseudo)populations in the excited states (column 4) are the coefficients linking number densities in a sublevel (column 5) to the total number density n_m or $n_m^{(4)}$ in the 2^3S state. Column 6 lists the notations for the normalised velocity distributions, where v_z is the atomic velocity component on the light propagation axis.

written as

$$\hat{\gamma}_{pq}(v_z) = \hat{K} I_{\text{pr.}} \hat{T}_{pq} \times \int d\nu \mathcal{F}(\nu - \nu_{\text{pr.}}) \mathcal{L}_W \left[\nu - \frac{\hat{\epsilon}_{pq}}{h} \left(1 - \frac{v_z}{c} \right) \right] \quad (13)$$

in which \hat{T}_{pq} are the transition matrix elements that represent T_{pq} or $T_{pq}^{(4)}$ for pump light absorption and $^*T_{pq}$ or $^*T_{pq}^{(4)}$ for probe light absorption, and \mathcal{L}_W is a normalised Lorentzian distribution of full width at half maximum (FWHM) W :

$$\mathcal{L}_W(\nu - \nu') = \frac{2/(\pi W)}{1 + [2(\nu - \nu')/W]^2}. \quad (14)$$

For the transition rate of Eq. 13, $W = \hat{\Gamma}'/2\pi$ is linked with the pressure-broadened damping rate of the L–H transition (cf. Sect. 2.3). The coefficient \hat{K} can be conveniently derived by noticing that each integral over v_z in the right-hand side sum of Eq. 12 is a convolution of normalised functions, and is thus a normalised function of the probe frequency. For an unpolarised gas with equally populated sublevels ($\hat{n}l_p = \hat{n}_L/g_L$, with \hat{n}_L the number density in the lower level), Eq. 12 can therefore be identified with the usual expression of absorption cross section [21]¹

$$\sigma_a(\nu_{\text{pr.}}) = -\frac{1}{\hat{n}_L I_{\text{pr.}}} \frac{dI_{\text{pr.}}}{dz}(\nu_{\text{pr.}}) = \hat{\gamma} \frac{\lambda^2}{8\pi} \frac{g_H}{g_L} g(\nu_{\text{pr.}}) \quad (15)$$

¹The difference between Eq. 15 and the expressions used in Ref. [21] results from the fact that optical angular frequency ω is consistently used in that work, contrary to e.g., Ref [22] and this article in which the optical frequency ν is used. Ref. [21] was revised and some corrections were made in [23] but Eq. 15 remained unchanged.

where $\hat{\gamma}$ is the total rate of spontaneous emission from the higher level, $\hat{\lambda}$ the transition wavelength, and g a normalised line shape function. Summing relations like Eq. 9 over all higher sublevels but retaining only one of the three light polarisations yields $\sum_{p,q} \hat{T}_{pq}(e_\lambda) = g_H/3$, and the value of \hat{K} is derived

$$h\nu_{\text{pr.}} \hat{K} = \frac{3\hat{\lambda}^2 \hat{\gamma}}{8\pi}. \quad (16)$$

This can equivalently be expressed in terms of the absorption oscillator strength \hat{f} [21]:

$$h\nu_{\text{pr.}} \hat{K} = \frac{3g_L}{g_H} \frac{h\alpha \hat{f}}{2m_e}, \quad (17)$$

where α is the fine-structure constant and m_e the electron mass. The ratio $3g_L/g_H$ is equal to 1 for the 1083 nm transition and to 9 for the 706.5 nm transition.

These relations can be further simplified in several situations. For instance, when the sample is optically thin or when velocity distributions are sufficiently broad, absorption only affects the probe intensity $I_{\text{pr.}}(z)$, not its frequency distribution \mathcal{F} . In particular, if $\mathcal{F} = \mathcal{L}_\delta$ is a Lorentzian intensity distribution of width δ , the convolution in Eq. 13 simply yields a Lorentzian of width $W + \delta$:

$$\hat{\gamma}_{pq}(v_z) = \hat{K} I_{\text{pr.}}(z) \hat{T}_{pq} \mathcal{L}_{W+\delta} \left[\nu_{\text{pr.}} - \frac{\hat{\epsilon}_{pq}}{h} \left(1 - \frac{v_z}{c} \right) \right]. \quad (18)$$

The probe transmittance is finally derived by integration on z over the cell length, L_{cell} , of the right-hand side of Eq. 12 divided by $I_{\text{pr.}}$. This simply introduces spatial averages $\langle \hat{n}_{lp} \rangle$ of the probed sublevel atomic densities (or the spatial average $\langle \hat{n} \rangle$ if the populations are uniform, which is assumed in the following), and a polarisation-dependent spectral function noted \hat{S} :

$$-\ln \hat{\mathcal{T}} = L_{\text{cell}} \langle \hat{n} \rangle \frac{3\hat{\lambda}^2 \hat{\gamma}}{8\pi} \hat{S}(\nu_{\text{pr.}}), \quad \text{with} \quad (19)$$

$$\hat{S}(\nu) = \sum_{p,q} l_p \hat{T}_{pq} \int dv_z \phi_{Lp}(v_z) \mathcal{L}_{W+\delta} \left[\nu - \frac{\hat{\epsilon}_{pq}}{h} \left(1 - \frac{v_z}{c} \right) \right] \quad (20)$$

For thermal velocity distributions in unpolarised gas, which occur in a weak discharge in the absence of pump beam, the thermal spectral functions \hat{S}_{th} are linear combinations of Voigt profiles. For low gas pressure and narrow-band probe light ($W + \delta \ll \Delta$, with values of Doppler width listed in Table 3), \hat{S}_{th} approximately combines Gaussian profiles:

$$\hat{S}_{\text{th}}(\nu) \approx \frac{1}{\hat{\Delta} \sqrt{\pi}} \sum_{p,q} l_p \hat{T}_{pq} \exp \left(-\frac{(\nu - \hat{\epsilon}_{pq}/h)^2}{\hat{\Delta}^2} \right). \quad (21)$$

The scaled dimensionless quantities $\hat{\Delta} \sqrt{\pi} \hat{S}_{\text{th}}$ are plotted in Figs. 2c and 2d. For the 1083 nm transition this quantitative link between transmittance and number densities of absorbers in the relevant sublevels is indeed identical to that previously published [17, 22, 24]. It applies to

the 706.5 nm transition as well when replacing the generic parameters in Eqs. 19 and 21 with the specific ones.

When velocity distributions $\phi_{Lp}(v_z)$ depart from thermal equilibrium, \hat{S} retains the property that each integral over v_z is a normalised function of frequency, which means for instance that integration of resolved components of transmittance data can yield quantitative information on number densities in the corresponding sublevel. For instance, when the *D_0 line component is scanned in ^4He using any probe polarisation, the area $^*A_0^{(4)}$ of the absolute transmittance data is

$$\begin{aligned} ^*A_0^{(4)} &= - \int_{^*D_0} d\nu_{\text{pr.}} \ln ^*\mathcal{T}(\nu_{\text{pr.}}) \\ &= L_{\text{cell}} \langle n_m^{(4)} \rangle \frac{3^* \lambda^2 ^*\gamma}{8\pi} ^*T_{9k}^{(4)} z_9, \end{aligned} \quad (22)$$

where the index k depends on the choice of polarisation but all $^*T_{9k}^{(4)}$ are equal to 1/9 (see Table 5). For other lines, similar simple relations can be explicitly derived in particular for a π -polarised probe, a configuration experimentally studied in this work. When the *D_1 component is used, the populations z_6 and z_8 are probed with equal weights and

$$^*A_1^{(4)}(\pi) = L_{\text{cell}} \langle n_m^{(4)} \rangle \frac{3^* \lambda^2 ^*\gamma}{8\pi} ^*T_{61}^{(4)} (z_6 + z_8). \quad (23)$$

Similarly when the *C_n line components probe absorption by ^3He atoms in the 2^3P_0 level ($n = 8$ or 9)

$$^*A_n(\pi) = L_{\text{cell}} \langle n_m \rangle \frac{3^* \lambda^2 ^*\gamma}{8\pi} ^*T_{18,k} (b_{18} + b_{17}), \quad (24)$$

where $k = 5$ for $n = 8$ and $k = 2$ for $n = 9$.

These expressions relate probe absorption data to number densities of selected sublevels in the 2^3P state. Besides, the *total* number density in the 2^3P state can independently be linked with the absorbed pump intensity ΔI_P using simple detailed balance considerations involving the 2^3P decay rate and the wavelength of the pumping transition:

$$\Delta I_P = L_{\text{cell}} \left[\langle n_m \rangle \sum_{j=1}^{18} b_j + \langle n_m^{(4)} \rangle \sum_{j=1}^9 z_j \right] \gamma hc / \lambda. \quad (25)$$

Discharge-dependent parameters are thus eliminated when considering the ratios of any of the line areas $^*\hat{A}$ (Eqs. 22 to 24) to the absorbed pump intensity (Eq. 25), which yields

$$(^*\hat{A} / ^*\hat{T}_{jk}) / \Delta I_P = \frac{3^* \lambda^2 ^*\gamma \lambda}{8\pi \gamma hc} \hat{\mathcal{R}} \quad (26)$$

$$\text{with } \frac{3^* \lambda^2 ^*\gamma \lambda}{8\pi \gamma hc} = 8.843 \text{ MHz cm}^2 \text{ mW}^{-1}, \quad (27)$$

where $\hat{\mathcal{R}}$ is the fraction of the atoms in the 2^3P state which are in the probed sublevel(s), e.g., $\hat{\mathcal{R}}_0 = z_9 / \sum_{j=1}^9 z_j$ for a probe scanning the *D_0 line in pure ^4He .

When the pump intensity is weak enough to induce negligible atomic alignment or orientation (population differences) in the 2^3S state and small enough populations in the 2^3P state (therefore negligible stimulated emission), an exponential intensity decrease results from light absorption in the gas. In that limit, the absorbed pump intensity linearly scales with the average pump intensity as

$$\Delta I_P^{(\text{lin})} = -\ln \mathcal{T}_0 \langle I_P \rangle \quad (28)$$

where \mathcal{T}_0 is the null-intensity limit transmittance of the pump beam. When Eq. 28 is substituted in Eq. 26, a linear increase of the areas $^*\hat{\mathcal{A}}$ with the average pump intensity is obtained in the weak-pumping limit. It involves the factor in Eq. 27 and the fraction $\hat{\mathcal{R}}$ which is of the order of 1 at low enough pressure:

$$^*\hat{\mathcal{A}}^{(\text{lin})} = -\ln \mathcal{T}_0 \hat{T}_{jk} \hat{\mathcal{R}} \frac{3^*\lambda^2 \gamma \lambda}{8\pi \gamma h c} \langle I_P \rangle. \quad (29)$$

This sets the scale for the expected optical signals and is used for comparisons with experimental data.

2.3 VSOP and probe absorption linewidth

Velocity-selective optical pumping (VSOP, [25]) is the key first step of double optical resonance. With a narrow pump laser tuned close to an atomic resonance, only atoms with velocity projections close to zero are excited with a significant rate from the 2^3S to the 2^3P state. Velocity distribution profiles in these two states may therefore strongly differ from thermal distributions. This is illustrated in Figs. 3b and 3c for the simple case of isolated pump and probe transitions in ^4He , namely with π -polarised pump light on the D_0 component (Fig. 3a).

The steady-state result of VSOP in helium can be described by the (position-dependent) populations and the associated normalised velocity distributions of the 2^3S and 2^3P sublevels, using the notations listed in Table 6. For the sublevels Y_2 and Z_9 directly addressed by the pumping light in Fig. 3a, typical velocity distributions are displayed in panels b and c, respectively. A narrow hole is burnt in the thermal velocity profile of the Y_2 level (a narrow peak correspondingly appears on top of thermal velocity profiles of levels Y_1 and Y_3 , not shown), while populations are modified ($a_2 < a_1, a_3$). In contrast, the velocity distribution in the 2^3P state mostly results from the VSOP process, with a negligible thermal contribution from the radiative cascade in a weak discharge: it is characterised by a narrow peak with a negligible broad pedestal.² These usual features of VSOP are directly relevant for the Doppler-free spectroscopy performed in this work, since the linewidth $\Delta^*\nu$ of 706.5 nm light absorption

²In our experimental conditions, probe absorption in the absence of pump light was too weak to be detected. Additionally, the pump beam was mechanically modulated and pump-induced probe absorption difference was extracted using lock-in detection.

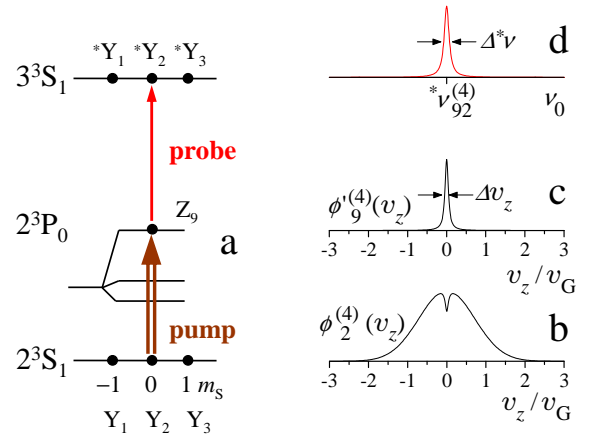


Figure 3: a: Example of double optical resonance scheme in ^4He using π -polarised pump and probe tuned to the D_0 and *D_0 transitions, respectively. b, c: VSOP-controlled velocity distribution profiles in the Y_2 and Z_9 sublevels addressed by the pump (notations are defined in Table 6). d: Absorption spectrum for the 706.5 nm probe scanning the *D_0 line. The velocity and frequency widths are discussed in the text.

signals (Fig. 3d) partly results from the velocity distribution width Δv_z of atoms in the probed 2^3P_0 level.

If the pump intensity I_P is low enough, Δv_z solely results from the combination of the natural linewidth of the 1083 nm transition, of its pressure broadening, and of the pump laser spectral width δ . If the latter is assumed to have a Lorentzian profile, all contributions simply add up to yield the FWHM of the velocity profile for $I_P = 0$

$$\Delta v_z|_{I_P=0} = \lambda [\gamma + 2w + 2\pi\delta] / 2\pi. \quad (30)$$

In Eq. 30 the wavelength λ of the pump converts frequencies to velocities, γ is the radiative decay rate in the 2^3P state ($\gamma/2\pi = 1.626$ MHz [26, Table 14]) and w is the pressure-dependent collision broadening rate ($w/\pi \approx 12$ to 18 MHz/mbar [9, 24]). The line shape of the 706.5 nm absorption signal is a narrow Lorentzian profile which results (by convolution) from the velocity distribution profile in the pumped 2^3P level and the linewidth of the probed transition itself. Its total width is therefore the sum of two terms, here expressed in frequency units:

$$\Delta^*\nu|_{I_P=0} = \Delta v_z|_{I_P=0} / ^*\lambda + \Gamma'_{706}/2\pi. \quad (31)$$

The first part involves the width of the velocity distribution of atoms excited by the pump light obtained in Eq. 30, converted to frequency using the wavelength $^*\lambda$ of the probe. The second part, $\Gamma'_{706}/2\pi$, combines widths arising from the radiative lifetimes of the 2^3P state ($\gamma/2\pi$) and of the 3^3S state ($^*\gamma/2\pi = 4.425$ MHz [26, Table 14]), collisional broadening of the 706 nm transition (33 MHz/mbar, [14]), and the instrumental linewidth of the probe laser. Altogether, the expected FWHM is the sum of contributions due to the radiative lifetimes (6.92 MHz), collisional broadening (52 to 61 MHz/mbar), and laser widths

(typ. 7.5 MHz for pump and probe lasers having 3-MHz widths), adding up to $\Delta^*\nu|_{I_P=0} = 22$ MHz for 0.13 mbar, the lowest pressure used in our experiments.

At sufficient pump intensity, power broadening arising from saturation of the transition and from the creation of holes in velocity profiles is well documented for simple two-level systems [27]. Dedicated OP models are needed in the case of helium to establish a quantitative link between pump intensity and broadening of the velocity profiles in the 2^3S and 2^3P states. Such models usually involve a coarse phenomenological treatment of collisions and of relaxation [17, 28, 29] and their use to evaluate velocity profiles falls beyond the scope of this article. Let us only mention that pressure broadening of the velocity distribution is expected to retain its generic expression as a function of the pump intensity I_P :

$$\Delta v_z = \sqrt{1 + I_P/I_{\text{sat}}} \Delta v_z|_{I_P=0}, \quad (32)$$

where, however, I_{sat} is an effective saturation intensity which depends on various parameters in the OP model.

2.4 Zeeman effects in double optical resonance

In this section generic notations are used to correspond to ^3He or ^4He , but the higher and lower states are implied by the choice of the pump or probe transition. Considering a pump-induced transition from L_i to H_j , with average pump frequency ν_P and level energy difference $h\hat{\nu}_{ij}$, the pump detuning $\hat{\nu}_{ij} - \nu_P$ selects atoms in the 2^3S state which are suitably Doppler-shifted. Their average velocity v_z^S and the corresponding velocity of the atoms in the 2^3P state are linked by

$$v_z^P - v_{\text{recoil}} = v_z^S = (\hat{\nu}_{ij} - \nu_P) \lambda \quad (33)$$

where the recoil velocity $v_{\text{recoil}} = h/(\hat{M}\lambda)$ amounts to 12.3 and 9.2 cm/s for ^3He and ^4He , respectively (\hat{M} is the atomic mass). For a $2^3\text{P}-3^3\text{S}$ transition frequency $^*\hat{\nu}_{jk}$ from L_j to H_k the probe frequency ν_0 needed for resonant absorption by atoms with the pump-selected velocity of Eq. 33 satisfies

$$^*\hat{\nu}_{jk} - \nu_0 = v_z^P/^*\lambda = (\hat{\nu}_{ij} - \nu_P) \lambda/^*\lambda + h/(\hat{M}^*\lambda\lambda). \quad (34)$$

The Zeeman shift of the resonant probe absorption frequency ν_0 in an applied field B is obtained as the difference of values obtained using Eq. 34 for B and a null field. In that operation, the actual value of the pump frequency and the recoil term both cancel out, and the shift is

$$\nu_0(B) - \nu_0(0) = ^*\hat{\nu}_{jk}(B) - ^*\hat{\nu}_{jk}(0) - \lambda/^*\lambda [\hat{\nu}_{ij}(B) - \hat{\nu}_{ij}(0)]. \quad (35)$$

The frequency differences in the right-hand side of Eq. 35 are conveniently expressed writing the linear B -dependency of the energies as a function of the \hat{m} quantum numbers in the three involved sublevels, characterised by

the three indices i , j , and k , so that the linear Zeeman shift factor is

$$\frac{\nu_0(B) - \nu_0(0)}{B} = \left[\frac{\lambda}{^*\lambda} \hat{g}_1(i) \hat{m}_1(i) - \frac{\lambda + ^*\lambda}{^*\lambda} \hat{g}_2(j) \hat{m}_2(j) + \hat{g}_3(k) \hat{m}_3(k) \right] \mu_B \quad (36)$$

where \hat{g}_1 , \hat{g}_2 , and \hat{g}_3 are the g -factors (g_F for ^3He , g_S or g_J for ^4He) of the involved sublevels of the 2^3S , 2^3P , and 3^3S states, respectively, and \hat{m}_1 , \hat{m}_2 , and \hat{m}_3 their angular momentum projections. Note that the signs in the weights affecting the contributions of the energy shifts in the three states in Eq. 36 are those obtained for the co-propagating beam configuration; different weights would be derived for a counter-propagating scheme, not used in this work.

Equation 36 can be explicitly written for any pump and probe line component, using the values of g -factors listed in Table 1 and immediately after Eq. 4. For the simple scheme involving the 2^3P_0 state of ^4He depicted in Fig. 3a it reduces to

$$\frac{\nu_0(B) - \nu_0(0)}{B} = \left[\frac{\lambda}{^*\lambda} m_S + ^*m_S \right] g_S \mu_B. \quad (37)$$

For a π -polarised pump ($m_S = 0$ is selected), a triplet of absorption lines can potentially be observed (depending on the probe polarisation) with the usual $^*g_S \mu_B$ splitting factor (28 MHz/mT). Conversely, for a fixed π -polarisation of the probe ($^*m_S = 0$), three velocity classes can potentially be excited (depending on the pump polarisation) and a triplet of absorption lines can also be observed, with an enhanced splitting factor, $g_S \mu_B \lambda / ^*\lambda$ (42.9 MHz/mT). Altogether, when all possible pump and probe polarisations are considered, nine lines may be observed with unevenly spaced shift factors spanning ± 70.9 MHz/mT.

3 Experimental setup and protocol

The main elements of the double optical resonance experiments lying in the same vertical plane are displayed in Fig. 4: the pump and probe lasers, the co-propagating beams overlapping in the experimental cell C_{exp} , the light polarisation and intensity control elements, and the saturated absorption setup which uses part of the pump beam and the ancillary cell C_{lock} . They are successively described in this section, along with off-plane light beams and elements. The setup had a 1.8×0.5 m² footprint.

Cells – Experiments were performed at room temperature with helium gas in sealed cylindrical Pyrex glass cells. Their dimensions ranged from 3 to 12 cm in length, 1.5 to 5 cm in diameter. The filling pressures ranged from 0.13 to 67 mbar of ^3He , ^4He , or isotopic mixtures. The cells had been made in-house for previous experiments according to a standard cleaning and filling protocol [17, 24]. They were positioned with a small tilt angle with respect to the

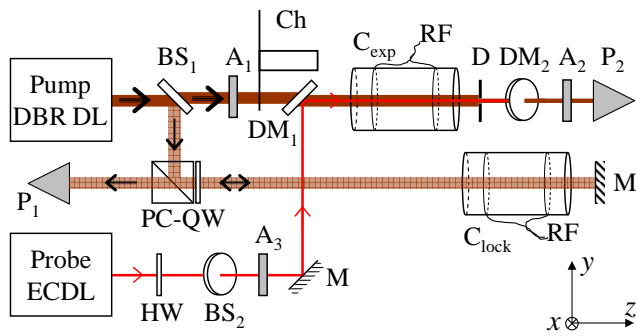


Figure 4: Schematic view of the main optical elements used in double optical resonance experiments (in the vertical yz plane, not to scale). The labeled components are 10% beam samplers (BS), absorptive attenuators (A), long-pass dichroic mirrors (DM), a polarising beam splitting cube with adhered quarter-wave plate (PC-QW), a half-wave plate (HW), and mirrors (M). The optical chopper (Ch) and the iris diaphragm (D, 2.3 mm^2 area) control beam propagation and diameter. Photodiode detectors (P) monitor beam powers. C_{exp} is the main experimental gas cell, C_{lock} the ancillary cell used to lock the pump frequency on an atomic transition. Additional elements lying outside the yz plane of the figure (probe wavelength measurement, transmitted probe polarisation analysis and detection, and power measurement) as well as the coil systems for B -field control are not displayed but are described in the text.

light beams to avoid large overlap from the reflections on the uncoated cell windows. A weak RF discharge was used to populate the 2^3S state with external wire electrodes arranged according to the cell shape. The RF frequency was of order 2–3 MHz or 20–25 MHz, depending on cell size and gas pressure. Low RF frequencies usually provided stable operation for weak discharges and lower RF interference noise whereas higher frequencies were used for easier discharge ignition at the lowest gas pressures. C_{exp} was located at the centre of the coil sets and C_{lock} was 7.5 cm lower and further along z so as to practically eliminate RF crosstalk and couplings of discharge intensities between cells.

Magnetic-field coils – A set of six square coils, similar to that used in Ref. [30], was used to apply an axial magnetic field component B_z up to 4 mT, with a computed relative field standard deviation (SD) of 7×10^{-5} over the probed volume in a 12-cm-long experimental cell. Two pairs of rectangular coils were used to apply field components transverse to the light beams, B_y (vertical) and B_x (horizontal, perpendicular to the plane of Fig. 4) with magnitudes up to 2 mT and computed SD of 1.3×10^{-3} and 2×10^{-3} , respectively, over the same probed volume. Details on the coil design, construction, and computed field maps can be found in Ref. [31]. The coil sets were used to cancel the unwanted Earth’s field components and to control the total field direction and magnitude in the experiments.

Pump laser – The laser source for the 1083 nm pump beam was a distributed Bragg reflector (DBR) diode laser (DL) with on-chip thermistor and thermoelectric cooler (Toptica LD-1082-0070-DBR) delivering 50 mW at our maximum operating current. The beam was collimated using an aspheric lens of 8 mm focal length. It was linearly polarised, with a polarisation vector along x (perpendicular to the plane of Fig. 4). The pump beam was mapped at the cell location ($0.2 \times 0.7 \text{ cm}^2$ FWHM) using a beam profiler (Thorlabs BC106N). Its on-axis maximum intensity inside the cell ($\approx 90 \text{ mW/cm}^2$) was fairly uniform over the area selected by the cropping diaphragm (labelled D in Fig. 4). It was evaluated taking into account the reflectance of the cell windows (typ. 9% per window). The sample transmittance for various pump intensities was inferred from pairs of pump power measurements after the cropping diaphragm with RF discharge on and off.

In some experiments, the pump laser was used in free-running operation, with its frequency set by the choice of the operating current and temperature (regulated using an in-house DL controller). To conveniently monitor pump absorption by the He gas in the cells, the discharge RF amplitudes could be modulated (around 80 Hz). Corresponding lock-in demodulation of signals from P_1 and P_2 was then performed and outputs similar to the sketch in Fig. 3b (see Fig. A.3) were obtained for P_1 during pump frequency scans.

In other experiments, the pump laser frequency was locked on a helium transition using a standard saturated absorption scheme applied to gas contained in the ancillary cell C_{lock} (Fig. 4). A small modulation of the DL current at 1.5 kHz was used to induce a pump frequency modulation, and lock-in demodulation provided a suitable error signal for a servo loop. The use of a quarter-wave plate allowed for convenient separation of the reflected beam by the PC-QW element after a double pass in C_{lock} . Moreover circularly polarised light yielded fewer (or single) line components in Zeeman spectra and therefore better frequency locking schemes. For most experiments with a locked pump laser, a mixture cell (with 1.07 mbar ^3He and 0.53 mbar ^4He) was used to lock on any of the three ^4He lines or on the ^3He C_8 line.

Probe laser – The laser source for the 706.5 nm probe beam was an extended cavity diode laser (ECDL, Toptica DL 100 L). We used a second in-house DL controller to manage the DL temperature and current, and computer control of the current and of the high voltage applied to the piezo actuator of the grating mount. Empirically determined joint linear variations of these current and voltage allowed for mode-hop-free tuning across the full helium spectra ($> 40 \text{ GHz}$, see Fig. 2c). This range exceeds the nominal specifications (21 GHz), which was sometimes convenient for wide frequency scans. However large amplitude noise was often observed near the boundaries of the scanned spectra and such large frequency intervals involved large changes in the DL current, thus in the probe amplitude. Therefore, suitable DL temperature adjust-

ments were routinely used to centre the scanned intervals on regions of interest in the absorption spectra. For a DL current close to the maximum operating value at the lower frequency, the probe power decreased by about 30% at the higher frequency of typical 15 GHz scans.

Probe wavelength measurement – The probe wavelength was monitored using a Fizeau wavemeter (High-Finesse WS6-600). Its fibre input (not shown in Fig. 4) collected light deflected by the beam splitter BS₂ in a horizontal plane. The recorded vacuum wavelength values $^*\lambda$ were used to compute frequency offsets $^*\nu$ using our nominal offset ($^*\varepsilon_0^{(4)}/h$ in Table 2) and the published vacuum wavelength³ $^*\lambda_0$ of the *D_0 transition:

$$^*\nu = ^*\varepsilon_0^{(4)}/h + c(1/^*\lambda - 1/^*\lambda_0) \quad (38)$$

$$^*\lambda_0 = 706.76568 \text{ nm}. \quad (39)$$

The wavemeter absolute accuracy was 600 MHz, but its specified resolution (20 MHz) and its readout resolution (10^{-5} nm, hence 6 MHz at the probe wavelength) could yield fairly precise measurements. Characterisations of its measurement errors were performed and are described in Appendix A. As expected for a Fizeau interferometer, the readout wavelengths remained quite stable, with corresponding frequency drifts not exceeding 10 MHz during a relevant scan time interval (10 to 30 s) when the probe laser frequency was not swept.

In spite of this fair time stability of the readout data, recordings performed for swept lasers frequencies indicated that instrumental errors of tens to hundreds of MHz varied with the laser frequency, an observation similar to that recently reported for a high-accuracy device [33]. Such frequency dependent errors induced local scaling errors, not exceeding $\pm 5\%$, affecting for instance the obtained line widths or areas. These errors were usually reproducible for successive repeated recordings, but lost their correlations for recordings made hours or days apart. Averaging results of distant measurements may therefore be used to reduce the effect of the wavelength-dependent readout errors on line width and line splitting measurements.

Probe light detection – A general-purpose optical polarimeter (not shown in Fig. 4) included a polarising beam splitting cube (and an additional polariser in the deflected channel) for separation of the horizontal and vertical polarisation components of the probe light (H and V, aligned with x and y in the measurement cell, respectively) [34, 35]. The split beams were coupled by $f = 30$ mm lenses into 1-mm core multimode plastic fibres that channelled light to Si PIN photodiodes (Siemens

BPW34), and photocurrents were suitably converted to voltages. This light collecting scheme for the photodetectors P_H and P_V provided a high directional selectivity and made detection immune to stray light. It was used for the 1083-nm-sensitive detector P₁ (Siemens BP104F) as well, whereas a large area photodiode (Centronic OSD50-4X, P₂) was directly placed on the path of the pump beam.

The direction of the linear polarisation of the probe light was rotated using a half-wave plate HW. Only horizontal or vertical polarisations in cell C_{exp} (characterised by null signals from detectors P_V and P_H, respectively) were used in standard experiments. They were fully preserved by the dichroic mirrors DM₁ and DM₂ and were thus well defined in the experimental cell. Therefore, for a transverse applied magnetic field along the direction of the linear light polarisation (π -polarised light), only $\Delta m = 0$ transitions were excited or probed. Otherwise σ -polarised light was obtained for field directions perpendicular to that of the light polarisation (with equal intensities of σ_+ and σ_- components), driving $\Delta m = \pm 1$ transitions. Combinations of π and σ polarisations, achieved for slanted orientations of the field in the transverse plane, were used in some experiments.

Data acquisition – For a standard experiment, the pump frequency was fixed and locked to an atomic transition unless otherwise specified. The pump intensity was varied using attenuators. The pump intensity in the sample and that absorbed by the sample were inferred from power measurements with discharge off and on (performed at low pump intensities using the photodetector P₂). For fixed discharge and pump settings, the probe laser frequency was linearly swept over a chosen interval, either in single pass or periodically for several scans. Probe frequency sweep rates of 200 MHz/s or slower were normally chosen, depending on the linewidths of the probed transitions.

During recordings the pump beam intensity was modulated (at 1.5 kHz) using a rotating wheel optical chopper. The signals from the photodetectors P_H and P_V were demodulated using digital lock-in amplifiers (Signal Recovery / EG&G 7220). An output time constant of 20 ms (6dB/octave) was usually chosen. The raw photodetector signals were also integrated with simple RC networks to filter out the modulation, and both the integrated and the demodulated signals were digitally recorded. A 16-bit USB data acquisition ADC module (Data Translation DT9816) with a 1-kHz sampling rate was managed by an in-house program that simultaneously controlled the probe laser frequency via a 12-bit DAC module (DT9813). Decimation of the oversampled data was performed in post-processing. Digital or aliased noise resulting from the digital data recording were thus made negligible. The variations of the probe wavelength (vacuum wavelengths versus time) were simultaneously recorded using the proprietary software of the wavemeter. The probe beam was transiently blocked at the beginning of each recording, which provided a time stamp used in data processing to

³In the text we have used the traditional designation 706.5 nm for the transition wavelength, which refers to the mean air wavelength [12, 13, 14, 15, 16]. The vacuum wavelength in Eq. 39 is indeed larger and can be obtained from the difference of level energies given in cm^{-1} in the NIST database [32] or in MHz in Ref. [18, Table 6]. The corresponding energy values in Ref. [26, Table 14] are slightly different, with a vacuum wavelength equal to 706.7657 nm. This difference, corresponding to a 12 MHz frequency shift, lies beyond the accuracy of our current wavelength measurements.

accurately align optical and wavelength data and eliminate time.

4 Results

4.1 Examples of double optical resonance spectra

Illustrative examples of double optical resonance experimental spectra are compared in this section. The probe transmittance $^*\mathcal{T}$, which can be directly linked with the atomic density distributions of velocities in the 2^3P state sublevels (Secs. 2.2 and 2.3), was computed for each photodetector (P_H or P_V) from the ratio of demodulated signal magnitudes, V_{RMS} , and averaged signal levels, V_{av} , as

$$^*\mathcal{T} = [1 - \beta V_{\text{RMS}}/V_{\text{av}}] / [1 + \beta V_{\text{RMS}}/V_{\text{av}}]. \quad (40)$$

This approach is reminiscent of that used in the case of weakly modulated densities of absorbers [24, App. A], but in this experiment the density of 2^3P -state absorbers was fully modulated with a near-square time pattern. For negligible rise and fall times of the pump intensity the coefficient in Eq. 40 would be $\beta = \pi/(2\sqrt{2})$. The effect of the finite transition times introduced by the pump beam chopper was assessed on the signals from the pump photodetector P_2 . As a result the corrected value $\beta = 1.03\pi/(2\sqrt{2})$ was used.

In order to conveniently compare recorded transmittance spectra to theoretical expectations, frequency offsets (i.e. shifts from the $^*\text{C}_1$ line) were inferred from wavelength measurements in two steps. Recorded wavelength data were first suitably processed to reduce spurious noise and interpolation of the processed data was used to ascribe a wavelength value to each computed transmittance value. The corresponding experimental frequency offset was then obtained using Eq. 38.

Figure 5 displays examples of double optical resonance data selected to show the effect of the gas composition and pressure on the observed absorption spectra. For the top row (Figs. 5a to 5c), the pump selectively excited each of the three J -levels of the 2^3P state of ^4He . Absorption of the probe predominantly occurred from the pumped level, as expected. The weak absorption signals corresponding to atoms in the unpumped levels (note the 10-fold gain factor on one side of the broken axis in Figs. 5a to 5c) result from small population transfers induced by J -changing collisions during the 2^3P state radiative lifetime. For the experiments of Figs. 5d and 5e, the 2^3P_0 levels of ^4He and ^3He were excited in the same cell using the well-resolved D_0 and C_8 pumping transitions, respectively. Narrow lines still correspond to absorption by atoms and isotopes selectively promoted to the pumped levels, and signals corresponding to absorption by atoms in the un-pumped levels are more salient than at lower pressure, as expected. With the large signal-to-noise ratio available in these measurements (the typical standard

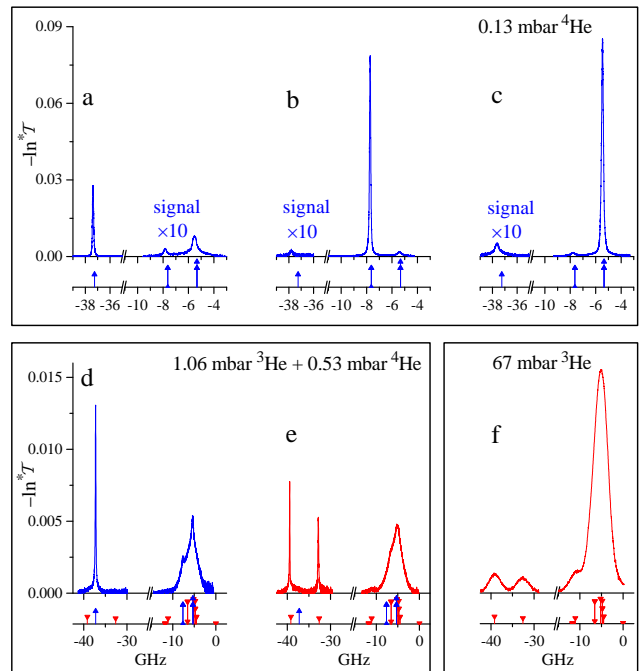


Figure 5: Experimental double optical resonance spectra in low-pressure ^4He (a to c), an isotopic mixture (d and e), and high-pressure ^3He (f). The gas pressure and composition is indicated in each box. Transmittance data are plotted vs. probe detuning from $^*\text{C}_1$. The pump frequency was tuned to: D_0 (a), D_1 (b), or D_2 (c) for pure ^4He ; D_0 (d) or C_8 (e) for the mixture; C_3 (f) for pure ^3He . The on-axis pump intensity incident on the cell was 55 mW/cm^2 (a to c) or 0.1 W/cm^2 (d to f). Relevant transition matrix elements from Figs. 2a and 2b are displayed below each spectrum. Note the different transmittance and frequency scales for the top and bottom rows. The displayed frequency ranges add up to 12 GHz (top) and 35 GHz (bottom).

deviation in the baselines was 5 to 9×10^{-5}), the transition frequencies could be inferred with a small statistical uncertainty ($0.1 - 1 \text{ MHz}$). The agreement with the computed frequency offsets (depicted as vertical bars below each spectrum) was usually fair but significant discrepancies (tens to hundreds of MHz) were often found (for instance in Fig. 5b for the main line and in Figs. 5b and 5c for the weak lines). This issue is discussed in Appendix A and illustrated in Sect. 4.4.

The high-pressure absorption data in Fig. 5f show no evidence of narrow features, but resemble a computed Doppler-broadened spectrum (Fig. 2c). However, attempts (not shown) to fit absorption data using computed spectra revealed sizeable deviations in line shapes unless Voigt (rather than Gaussian) profiles were used, as expected, and a slightly weaker weight was ascribed to the 2^3P_0 population.

The total populations of the various levels of the 2^3P state and population-transfer collision rates may be inferred from areas of line components in such data. Glob-

ally, 80 to 90% of the 2^3P population lied in the pumped state and velocity class for the low-pressure experiments (Figs. 5a to 5c). In contrast, only 25% remained in the pumped 2^3P_0 velocity class for the 1.6 mbar gas mixture (Figs. 5d and 5e), and 10% (close to the thermalised limit of 1/9) of the atoms were detected in the un-pumped 2^3P_0 level for a 67 mbar ^3He gas submitted to excitation to the 2^3P_2 and 2^3P_x levels (Fig. 5f).

The $B = 0.16$ mT applied field was transverse and such that $B_y = 2B_x$ for the experiments on low-pressure ^4He . The pump light had thus equal intensity components on each of the three light polarisation states (σ_+ , σ_- , and π), which efficiently prevented OP-induced build-up of atomic alignment in the 2^3S state. This yielded an increase in both pump and probe absorption signals by a factor ~ 2 compared to field orientations corresponding to a π - or σ -polarised pump having the same total intensity. For experiments in cells containing sizeable amounts of ^3He (e.g., Figs. 5d to f), ME collisions with spin-1/2 ground state atoms efficiently prevented alignment to occur in the 2^3S state and absorption of pump and probe light was indeed observed to be almost unaffected by the direction of the applied field.

4.2 Examples of Zeeman-split spectra

Figure 6 displays probe absorption spectra obtained in an applied longitudinal field when the 2^3P_0 state of ^3He (Fig. 6a) or ^4He (Fig. 6b) was pumped. The Zeeman shifts derived in Sect. 2.4 were used to compute the expected line positions represented below the spectra.

The ^3He line component shifts were obtained using Eq. 35. For C_8 pump and *C_8 probe all F -values are equal to 1/2 and only two excitation paths $\hat{m}_1 \rightarrow \hat{m}_2 \rightarrow \hat{m}_3$ are allowed for σ -polarised light: $\pm 1/2 \rightarrow \mp 1/2 \rightarrow \pm 1/2$, yielding a doublet with shift factors computed using Eq. 36 and noted $\pm\beta_8 = \pm 44.18$ MHz/mT. For the *C_9 probe, $F = 3/2$ in the upper level and four excitation paths are allowed, yielding a barely split strong doublet ($\hat{m}_3 = \pm 3/2$, shift factors $\pm\beta_{9,3} = \pm 2.54$ MHz/mT, $^*T_{17,4} = 0.0937$) and a weak doublet ($\hat{m}_3 = \pm 1/2$, $\pm\beta_{9,1} = \pm 34.84$ MHz/mT, $^*T_{17,2} = ^*T_{17,4}/3$). The recorded spectra exhibit the corresponding features in Fig. 6a, and sums of Lorentzian profiles (the red lines) accurately reproduce the experimental data. Four parameters were used in the fitting function \mathcal{F}_8 for *C_8 spectra, yielding values for the total line area $A_{8\text{fit}}$, the common width $W_{8\text{fit}}$, the field strength $B_{8\text{fit}}$, and a frequency offset $\delta_{8\text{fit}}$.

$$\mathcal{F}_8(\nu_0) = A_{8\text{fit}} [\mathcal{L}_{W_{8\text{fit}}}(\nu_0 - ^*\nu_8 + \delta_{8\text{fit}} + \beta_8 B_{8\text{fit}}) + \mathcal{L}_{W_{8\text{fit}}}(\nu_0 - ^*\nu_8 + \delta_{8\text{fit}} - \beta_8 B_{8\text{fit}})] / 2. \quad (41)$$

The fit value $B_{8\text{fit}}$ was found in good agreement with B_z , the 0.5% difference being lower than the possible scaling errors in frequency scale discussed in Appendix A. Three parameters were used in the fitting function \mathcal{F}_9 for *C_9 spectra: $A_{9\text{fit}}$, $W_{9\text{fit}}$, and $\delta_{9\text{fit}}$, while the nominal applied field B_z was used since the poorly resolved lines could not

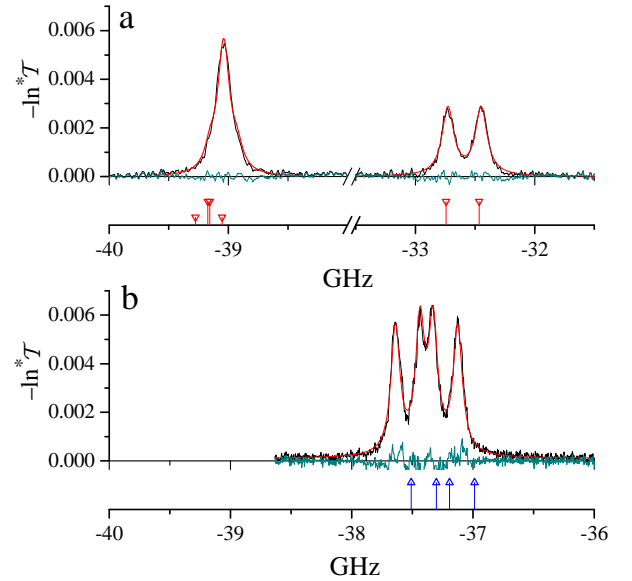


Figure 6: Double optical resonance spectra displaying combined Zeeman line splittings (σ -polarised pump and probe beams). a: Pump tuned to C_8 (55 mW/cm 2), $B_z = 3.14$ mT, $0.27+0.27$ mbar isotopic mixture. b: Pump tuned to D_0 (100 mW/cm 2), $B_z = 3.68$ mT, 0.133 mbar ^4He gas. Experimental data (black), Lorentzian fits (red, Eqs. 41 to 43), and residues (teal) are displayed. The bars below the spectra are the computed positions and transition matrix elements of the line components. Note the 4.5-GHz-long break in the frequency axis of panel a.

reliably yield both field and width fit values.

$$\mathcal{F}_9(\nu_0) = A_{9\text{fit}} [3\mathcal{L}_{W_{9\text{fit}}}(\nu_0 - ^*\nu_9 + \delta_{9\text{fit}} + \beta_{9,3}B_z) + 3\mathcal{L}_{W_{9\text{fit}}}(\nu_0 - ^*\nu_9 + \delta_{9\text{fit}} - \beta_{9,3}B_z) + \mathcal{L}_{W_{9\text{fit}}}(\nu_0 - ^*\nu_9 + \delta_{9\text{fit}} + \beta_{9,1}B_z) + \mathcal{L}_{W_{9\text{fit}}}(\nu_0 - ^*\nu_9 + \delta_{9\text{fit}} - \beta_{9,1}B_z)] / 8. \quad (42)$$

The frequency offsets $\delta_{8\text{fit}} = 17$ MHz and $\delta_{9\text{fit}} = 124$ MHz both lied within the precision of the frequency measurements (600 MHz). They differed from a common expected offset associated with the use of circularly polarised light to set or lock the pump laser frequency (Fig. 4). Such difference is discussed in more detail in Sect. 4.4. The linewidths $W_{8\text{fit}} = 119$ MHz and $W_{9\text{fit}} = 115$ MHz, each with a 2 MHz statistical uncertainty and a few % of uncertainty arising from possible scaling errors, are in satisfactory agreement. Finally, the ratio $A_{9\text{fit}}/A_{8\text{fit}} = 1.262$ of the line areas parameters was found to be consistent with the expected value, $(^*T_{17,4} + ^*T_{17,2})/^*T_{17,5} = 1.246$.

The ^4He shifts in Fig. 6b were obtained using Eq. 36. Four double resonance excitation paths through $m_J = 0$ are allowed for σ -polarised light: $m_S = \pm 1$ to $^*m_S = \pm 1$, yielding one doublet with shift factors $\pm\beta_{0l} = \pm 70.91$ MHz/mT, and $m_S = \pm 1$ to $^*m_S = \mp 1$, yielding another doublet with shift factors $\pm\beta_{0s} = \pm 14.91$ MHz/mT. A fitting function \mathcal{F}_0 for *D_0 with parameters $A_{0\text{fit}}$, $W_{0\text{fit}}$, $B_{0\text{fit}}$, and $\delta_{0\text{fit}}$

was used to model the Zeeman-split line in Fig. 6b:

$$\begin{aligned} \mathcal{F}_0(\nu_0) = & A_{0\text{fit}} \left[\mathcal{L}_{W_{0\text{fit}}} \left(\nu_0 - \nu_0^{(4)} + \delta_{0\text{fit}} + \beta_{0l} B_{0\text{fit}} \right) \right. \\ & + \mathcal{L}_{W_{0\text{fit}}} \left(\nu_0 - \nu_0^{(4)} + \delta_{0\text{fit}} - \beta_{0l} B_{0\text{fit}} \right) \\ & + \mathcal{L}_{W_{0\text{fit}}} \left(\nu_0 - \nu_0^{(4)} + \delta_{0\text{fit}} + \beta_{0s} B_{0\text{fit}} \right) \\ & \left. + \mathcal{L}_{W_{0\text{fit}}} \left(\nu_0 - \nu_0^{(4)} + \delta_{0\text{fit}} - \beta_{0s} B_{0\text{fit}} \right) \right] / 4. \quad (43) \end{aligned}$$

Again, the fit value $B_{0\text{fit}}$ (1.5% lower than B_z) and the frequency offset $\delta_{0\text{fit}} = -138$ MHz were in line with expectations. The linewidth $W_{0\text{fit}} = 90$ MHz, which was obtained with a 1 MHz statistical uncertainty, cannot be directly compared at this stage with that obtained at a different pressure, for the other isotope, and with a different pump intensity. We still notice that, for the two 2^3S - 2^3P_0 pumping schemes considered here, two narrow velocity classes with identical widths can be observed for the atoms detected in the 2^3P_0 level (one class for each of the two magnetic sublevels in ^3He , two classes with opposite mean velocities in ^4He when the pump is tuned to the resonant atomic frequency for $B=0$). Therefore a single width parameter can be used in all fit functions, which yields robust fit results even if the Zeeman components are ill-resolved. We have thus a suitable tool for fits of narrow (Doppler-free) lines, from which areas and widths can be reliably extracted. The situation would be more complex for pumping schemes addressing different sublevels with different pumping rates, for instance.

4.3 Effect of pump intensity

The influence of pump light intensity on probe absorption signals was studied for several conditions of gas composition and pressure, as well as of pump light polarisation and frequency. The strength of probe absorption was characterised by the areas of the narrow spectral lines corresponding to directly pumped atomic sublevels in each experiment. The areas were usually obtained from fit parameters of suitable model functions. They were checked to be consistent with those obtained from numerical integration whenever spectral shapes and signal-to-noise ratio allowed for it, for instance at high pump intensity and low gas pressure.

Figure 7a displays data obtained in different cells for π -polarised pump and probe light, plotted as functions of average pump intensities $\langle I_P \rangle$ (which were computed assuming exponential decay along the pump path). A wide range of area values was obtained at fixed pump intensity, as could be noticed for instance in Fig. 5. The solid lines in Fig. 7a are the low-intensity areas of Eq. 29 computed for the experiments made in the low-pressure cell using the low-intensity transmittance \mathcal{T}_0 . They agree with the corresponding data (solid triangles) within 10% below a few mW/cm^2 , and the differences at higher intensities emphasize the strong loss of efficiency in populating the probed 2^3P state over most of the pump intensity range.

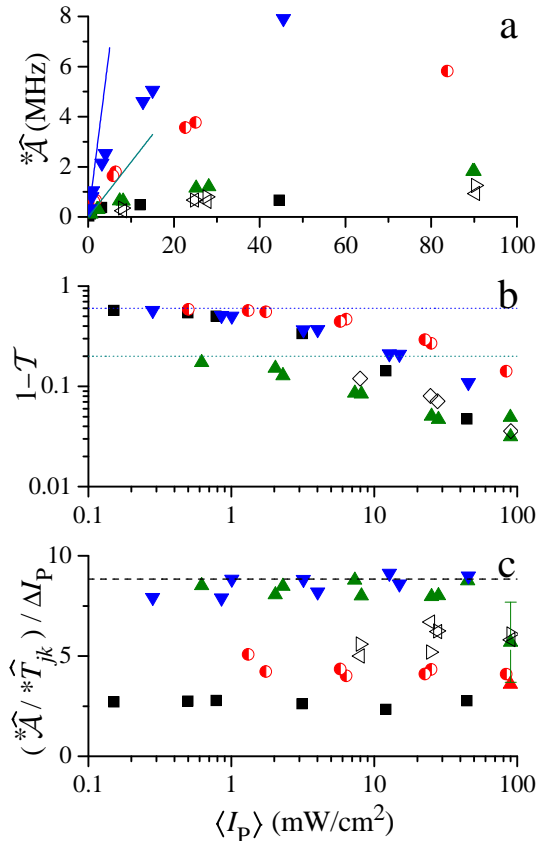


Figure 7: Series of data plotted vs. z -averaged pump intensities, for different gas samples and pumping lines: ^4He at 0.13 mbar (\blacktriangledown : D_1 , \blacktriangle : D_0) and 1 mbar (\blacksquare : D_0); ^3He at 0.4 mbar (C_8 pump, \triangleright : *C_8 probe, \triangleleft : *C_9 probe); ^4He at 0.4 mbar + ^3He at 0.13 mbar (\bullet : D_0). Plot a: Areas of narrow absorption lines corresponding to directly pumped 2^3P levels. The lines are computed areas for weak D_1 and D_0 pumps in the 0.13 mbar cell (Eq. 29 assuming $\mathcal{R} = 1$). b: Absorbed fraction of the pump intensity (\diamond : ^3He at 0.4 mbar). The dotted lines correspond to \mathcal{T}_0 values in the 0.13 mbar cell for very small I_P . c: Scaled ratios of Eq. 26. The dashed line is the value of Eq. 27. The choice of linear or logarithmic scales was made for clarity of presentation.

All area values tend to saturate at large pump intensity, which correlates with the decrease of pump absorption plotted in Fig. 7b for the corresponding experiments. It is worth noticing that the decrease with I_P was faster for pure ^4He (all solid symbols), in which atomic alignment was produced in the 2^3S state by π -polarised pump light. Optical pumping reduced absorption in that case, but it was efficiently hindered by ME collisions when ^3He or isotopic gas mixtures were used. Of course, enforcing equal intensities of the three pump light polarisation components (see Sect. 4.1) was another way to avoid optical pumping effects and to enhance absorption at large I_P in pure ^4He .

Figure 7c combines the results obtained for measured

areas (data of Fig. 7a) and measured pump intensity differences (between input and output of the gas samples), ΔI_P , as suggested by Eq. 26. The experimental errors for the areas mainly arose from frequency scaling errors (up to $\pm 5\%$) discussed in Appendix A. For the weakest absorptions at high I_P the accuracy on ΔI_P was rather poor as a result of large interference from the RF discharge (see a corresponding worst-case error bar in Fig. 7c). Allowing for these errors, the computed ratios were found to be quite independent of pump intensity for each sample, as expected. Moreover, their values were consistent with the expectation of Eq. 26, with fractions \mathcal{R} of atoms close to 1 at 0.13 mbar and decreasing with increasing pressure and collision rates (\mathcal{R} is the fraction of atoms in the 2^3P state which have remained in the pumped sublevel(s) and velocity class before radiative decay).

Investigations of optical pumping effects in the 2^3S state and of their consequences on the total populations in the 2^3P state could indeed solely involve pump absorption measurements, but 706.5 nm probe absorption measurements may yield higher accuracy especially in low-pressure samples. Moreover they provide additional information when the line shapes and widths are analysed, in addition to the line areas. A systematic compilation of the spectral data obtained in our experiments was performed. An overall increase of linewidths with gas pressure and a slow increase with pump intensity were observed. However, a so-far unexplained systematic deviation from the expected simple Lorentzian line shape was observed in low-pressure gas samples. Further investigations are needed before a comprehensive analysis can be reported.

4.4 Feasibility of Doppler-free spectroscopy

Following the conclusion of Appendix A, series of repeated scans of the 2^3P_0 - 3^3S transitions in isotopic gas mixtures were performed with the pump frequency locked to the C_8 or the D_0 line. The experiments were performed in null field to avoid Zeeman line shifts. Indeed, with linear pump and probe polarisations, Zeeman splittings (such as observed in Fig. 6) were not expected to affect centre-of-line positions. In contrast, the saturated absorption beam was circularly polarised and therefore the pump frequency would have been Zeeman-shifted proportionally to any B_z field. To avoid this, the three Earth's field components were compensated and in particular $|B_z| < 2 \mu\text{T}$, resulting in a worst-case frequency shift below 0.1 MHz in these experiments (Eq. 36).

Figure 8a displays the time variations of the probe wavelength and absorption spectra for six back and forth scans, for a C_8 -tuned pump. For each scan in a recording the *C_8 and *C_9 absorption lines were fit using Lorentzian profiles, yielding sets of fit frequencies, linewidths, and statistical uncertainties.

Fig. 8b displays the fit frequencies of the *C_8 transi-

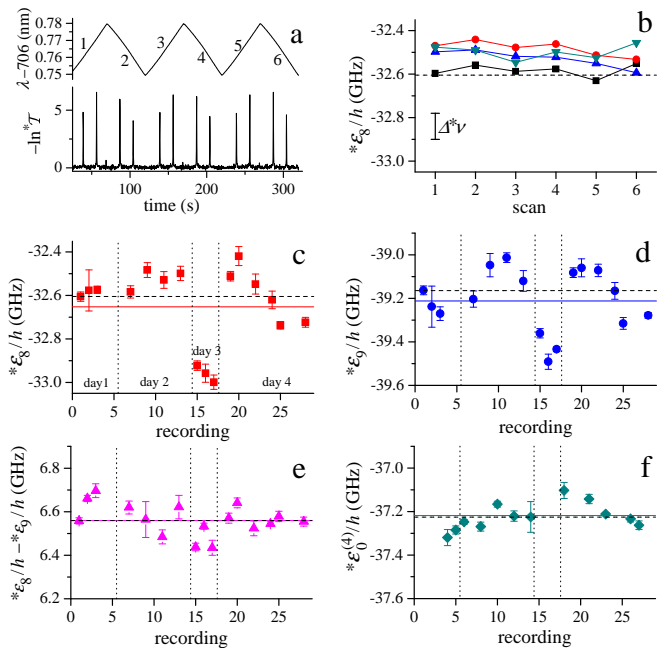


Figure 8: Results of series of repeated scans across the 2^3P_0 - 3^3S lines in isotopic mixtures with a pumped 2^3P_0 level. a: Typical recording comprising six scans for a C_8 -tuned pump. b: Fit absorption frequencies in a set of recordings are plotted vs. the scan number (squares: data from Fig. 8a; other symbols: three more recordings on the same day; connecting lines guide the eye for each recording). c, d, f: Averages (symbols) and standard deviations (error bars) of the six scans were derived for each recording. c and d: C_8 pumping, f: D_0 pumping. e: Difference of the data in c and d, yielding the hyperfine splitting in the 3^3S state of ^3He . The solid lines are the averages of all data, the dotted lines are the computed values (Table 2).

tion in Fig. 8a scans together with those from three more recordings made on the same day. The frequency drifts between scans of a recording or between recordings were on the same order of magnitude as the typical linewidth ($\Delta^*\nu = 120 \text{ MHz}$, vertical bar in Fig. 8b). The statistical uncertainty on fit frequencies ($\sim 1 \text{ MHz}$) was smaller than symbol sizes.

The results of all measurements for the *C_8 transition are compiled in Fig. 8c, in which the symbol positions and error bars stand for the averages and standard deviations of fit values obtained in each recording (the four recordings used in Fig. 8b yield the four data points of day 2). The results in Figs. 8c to 8e correspond to 29 recordings made on four different days using two cells with two gas mixtures: $0.27+0.27 \text{ mbar } ^3\text{He}+^4\text{He}$ on consecutive days 1 and 2, and $0.13+0.4 \text{ mbar}$ on days 3 and 4 one week later. The pump was tuned to C_8 to excite ^3He atoms (Figs. 8c to 8e, 17 recordings) or to D_0 to excite ^4He atoms (Fig. 8f, 12 recordings).

With similar plotting conventions Fig. 8e displays the differences in fit frequency for the *C_8 and *C_9 lines com-

puted for each scan recorded with C_8 pumping. The in-recording standard deviations (the error bars in Fig. 8e) and the scatter of average values of the line splittings are somewhat reduced compared to the absolute frequency measurements, but the frequency-dependent wavemeter errors were not eliminated in the process.

Table 7 lists the quantitative results of this series of measurements in terms of deviations from the computed values. The inferred hyperfine splitting in the 3^3S state of ^3He and isotope shift of the 706.5 nm transition are in good agreement with expectations in spite of the large and frequency-dependent readout errors of the wavemeter used in these experiments that make this instrument ill-suited for accurate spectroscopic measurements. The standard errors obtained for repeated measurements suggest that the measurement errors were in fact efficiently averaged.

line name	av. - th. (MHz)	SD (MHz)	SE (MHz)	N_s
* C_8	-38.1	177	18.5	92
* C_9	-39.7	144	15	92
* D_0	2.0	63.6	7.5	72
* $C_9 - C_8$	1.6	76.5	8	92

Table 7: Statistical data for the results compiled in Fig. 8. Columns 2 to 4 list the differences between the averaged fit frequencies and the computed values, the standard deviations and the standard errors of the fit frequencies. N_s is the number of scans used for each average. The last line contains the data for the ^3He hyperfine splitting measurements (see text and Fig. 8e)

5 Discussion

Calculations of the level structures and optical transition details for the 1083 nm transition of Ref. [17] were extended to the 706.5 nm transition. Explicit expressions of Zeeman shifts of the 2^3S , 2^3P , and 3^3S levels involved in double optical resonance are given in this article for the low-field limit, but this extension is indeed valid for arbitrary magnetic field using straightforward changes in the numerical computations of Ref. [17]. Regarding double optical resonance schemes, quantitative links were derived between integrated probe absorption spectra at 706.5 nm and atomic densities in the 2^3P state or pump absorption.

As regards line shapes, the low-pump-intensity limit was derived and the power broadening effects on velocity distributions in the 2^3S and 2^3P states were briefly discussed in Sect. 2.3. They would indeed automatically induce a related broadening of probe absorption lines. Additional broadening of the probe lines resulting from an intense pump may be expected for this 3-level ladder-type excitation scheme. Various theoretical approaches have

been used in similar situations (e.g., [36, 37, 38]). A pump-induced increase of the damping rate of the probe transition may be expected, with changes in the line shapes expected from Rabi oscillations driven by an intense pump in a dressed-atom approach. Such effects are not believed to play a significant role in our experiments where strong optical saturation was not achieved, but a dedicated study at higher pump light intensity would probably benefit from the use of optical probes on both optical transitions.

A simple experimental scheme was used with collinear pump and probe beams combined using dichroic mirrors. This restricted the beam light polarisations to being linear and either *s*- or *p*-polarised (horizontal or vertical polarisations in our setup). This was required to avoid strong modifications of the beam polarisations, which are well known for reflections on dichroic mirrors [39] and were observed in this work for the transmitted beam as well. Experiments requiring arbitrary beam polarisations could advantageously be performed with pump and probe beams propagating with a small angle to avoid complex compensation of the effects of dichroic mirrors, at the expense of a loss of compactness of the system and of imperfectly cancelled Doppler broadening.

Double optical resonance spectra recorded with our simple scheme over a wide range of pressures displayed very clear features, with narrow Doppler-free lines below a few millibars. In that case complex Zeeman splittings resulting from the interplay of the Zeeman shifts and pump-induced velocity selection were observed and found to agree well with expectations. This provides a basis for reliable analyses and fits of the observed spectra in applied magnetic fields, in which line shapes, widths, and positions of individual components can be reliably determined even in poorly resolved Zeeman structures. Conversely, above a few tens of millibars, broad thermal-like spectra provided evidence of efficient velocity-changing collisions during the radiative lifetime of the 2^3P state. The velocity-selective character of the pump was essentially lost but the tremendous increase in signal-to-noise ratio of this approach, compared to conventional absorption or fluorescence techniques, still makes our pump-probe scheme very useful. And indeed, for the studies in the intermediate pressure regime which have motivated these experiments, analyses of recorded spectra for suitable combinations of pump and probe frequencies and polarisations can be expected to provide a wealth of useful data. The reported observations of the influence of pump intensity on signal amplitudes already highlight the pressure dependence of the fractional transfer of populations, both in pure ^4He and isotopic mixtures. It also provides values for suitable pump intensities in various situations, with large enough probe absorption and moderate saturation broadening.

Incidentally, an intrinsic frequency-dependent measurement error of a Fizeau-type wavemeter was evidenced and characterized. The resulting limitation on the precision of spectroscopic measurements on the Doppler-free

706.5 nm transition was evaluated, with a 10 to 20 MHz statistical error on line positions in our feasibility study. This already yields improved determinations of the hyperfine structure constant and isotope shift of this transition compared to prior results [12, 13, 16]. However, obtaining spectroscopically useful results with accuracies not exceeding sub-MHz statistical errors in a single scan would require a more accurate wavelength measurement instrument or method in order to settle, for instance, the 0.55 MHz discrepancy between the published isotope shift differences of Eqs. 6 and 7. Suitable measurements could be performed using, for instance, a more accurate model by the same manufacturer (with a 60-fold smaller stated error) or a stable interferometer (of the kind used in Ref. [16] for He absorption spectroscopy at 706.5 nm or in Ref. [40] for the determination of the He isotope shift at 1083 nm).

Acknowledgements

We thank V. Fossati for contributions to exploratory steps of the experiments and A. Lemettré for enhancements of the B -field coils, performed in the frame of independent internships.

Authors contributions

G.T and P.J.N. designed and initiated the project. A.D. performed most of the reported experimental work and data analysis. P.J.N. performed the calculations and wrote the manuscript with input from all authors.

Appendix

A Characterisations of wavemeter measurement errors

Wavemeters based on Fizeau interferometers have a resolution and stability significantly superior to their absolute accuracy. This feature has been used by several groups to precisely lock lasers at fixed frequencies using devices that have the highest available accuracy (10 MHz instead of 600 MHz in our experiments) [41, 42]. In this Appendix we report on checks of the readout stability of our wavemeter at fixed laser frequency, then examine an ill-documented feature of readout errors for frequency-swept lasers, and illustrate the influence of such errors on measurements of well-known line component splittings for the 1083-nm transition.

A.1 Wavemeter readout stability

We have evaluated the time stability of measurement errors by monitoring readout drifts at fixed laser frequencies, for the un-swept probe laser sitting on a narrow dou-

ble optical resonance line, or for the locked pump laser (in that case, the photodetector P_2 was replaced with the collimator of the wavemeter input fibre). Slow read-out drifts were observed in both cases, and rapid changes were observed when the wavemeter input fibre was bent or moved or when the light injection into the fibre was geometrically modified. Figure A.1 displays an example of long-term recording of the wavemeter readout λ with the pump locked on the D_2 transition, of wavelength in vacuum λ_2 (from Ref. [32], see footnote before Eq. 39) given by

$$\lambda_2 = 1083.33064 \text{ nm.} \quad (\text{A.1})$$

The difference $\lambda - \lambda_2$ was of order 1.6 to 2.6 pm, i.e. 410 to 670 MHz in this example, which was consistent with the instrument accuracy (600 MHz). Short-term drifts (see the blow-up in Fig. A.1) during typical scan times in double optical resonance experiments (10 to 30 s) did not exceed 10 to 20 MHz, with a sub-MHz precision for smoothed data. The sudden noise increase and readout jump near the end of the recording were induced by small movements of the wavemeter input fibre.

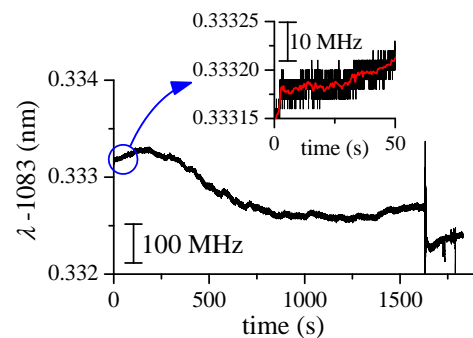


Figure A.1: Recording of wavemeter data for the 1083-nm pump DL locked on the ^4He D_2 line (of wavelength λ_2 : see text). The inset is a ten-fold blow-up of part of the recording, with raw data (black, 10 ms sampling) and smoothed data (red, 20-point running averages) achieving a sub-MHz precision.

A.2 Wavelength measurements for repeated scans of pump or probe lasers

In spite of this fair time stability of the readout error, recordings of readout wavelengths for swept lasers (both the pump and the probe) indicated that this instrumental error depended on the laser frequency. Figures A.2a and b display examples of deviations of the wavemeter readout values from expected linear variations with the pump laser frequency control parameter. Most recordings exhibit smooth variations (Fig. A.2a) but apparent jumps were sometimes observed (Fig. A.2b). The damped oscillations following each turning point in the triangular sweeps were actual DL temperature (and thus frequency) oscillations but the other features were variations in the wavemeter error similar to those recently reported for a

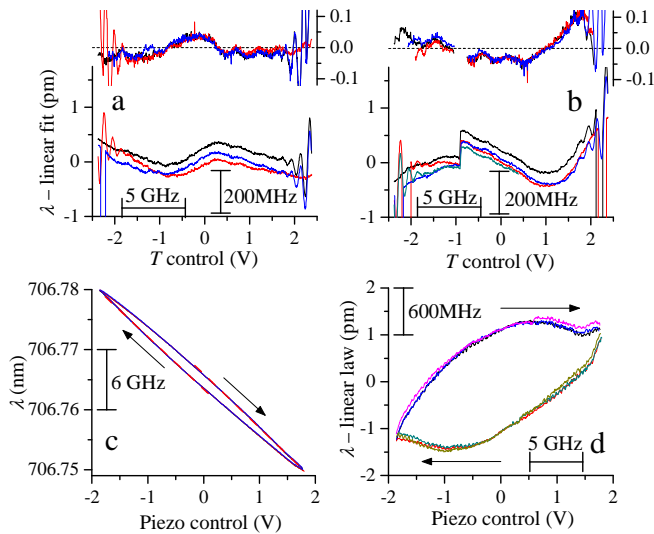


Figure A.2: Plots of processed data obtained from wavemeter readout values λ vs. the laser frequency control parameters (repeated back and forth scans appear in different colours). a,b: Pump laser at 1083 nm (vs the DL temperature control parameter). Lower traces: examples of deviations of λ from linear fits, with slopes s_λ , for the pump laser; Upper traces: derivatives of these deviations scaled to s_λ . c,d: Probe laser at 706.5 nm. c: Example of λ variation with the piezo actuator control for the probe laser. d: Corresponding differences to a linear law with the common slopes fit to the second halves of the hysteresis loops in c. The arrows in c and d indicate increasing times. Scale conversions to frequency units are displayed.

high-accuracy device [33]. The use of wavemeter data instead of the true wavelengths when processing absorption data therefore induced local scaling errors, given by the reduced derivatives of the deviations from linear variations, plotted as the upper traces in Figs. A.2a and A.2b. These scaling errors typically did not exceed $\pm 5\%$.

When the probe laser wavelength was recorded a clear hysteretic response was observed (Fig. A.2c). Subtracting a linear function of the control parameter (Fig. A.2d) did not suggest a reliable parametrisation for this behaviour, which was attributed to the mechanical response of the piezo actuator. We could therefore not avoid the local scaling errors resulting from the use of wavemeter data, and simply assumed that they had similar magnitudes at pump and probe wavelengths. These frequency-dependent errors were usually stable for successive recordings, which is evidenced by the rather similar traces within Fig. A.2a or Fig. A.2b. In contrast they lost their correlation for recordings made hours or days apart, as revealed by the differences between Figs. A.2a and A.2b.

A.3 Pump wavelength measurements for saturated absorption data

Simultaneous recordings of the 1083 nm pump wavelength and of saturated absorption signals from the ancillary cell (C_{lock} in Fig. 4) are reported here. Figure A.3 displays saturated absorption data and fitting steps for a frequency scan over the C_8 to D_1 lines in an isotopic mixture cell. The experimental frequency offsets were inferred from the recorded wavelength values using our nominal frequency offset ($\varepsilon_2^{(4)}/h$ in Table 2) and the wavelength in vacuum λ_2 (Eq. A.1) for the D_2 transition:

$$\nu = \varepsilon_2^{(4)}/h + c(1/\lambda - 1/\lambda_2). \quad (\text{A.2})$$

For convenience data processing consisted of two steps: the demodulated signals (left) were fit using Gaussian profiles and the residues (right) were fit using Lorentzian profiles. The positions of the saturated absorption dips, which had typical FWHMs of 20 MHz, were thus precisely inferred.

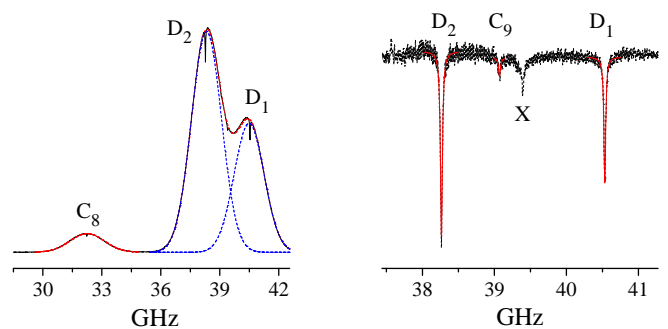


Figure A.3: Left: Demodulated saturated absorption signal from detector P_1 (see Fig. 4) with a modulated discharge amplitude in C_{lock} ($0.27+0.27$ mbar mixture) is plotted vs. the frequency offset from the C_1 transition (Eq. A.2). Sums of Gaussian profiles (dotted lines) were used to model thermal velocity distributions. Right: Expanded difference between the signals and the Gaussian fit for the right hand side of the spectrum. Three Lorentzian profiles were used to fit the saturated absorption dips. Atomic lines are labelled, X is the crossover resonance associated with D_1 and D_2 .

Series of recordings comprising three back and forth scans were repeated on four different days using two gas mixture cells. The line position fits from each scan were combined to compute the three line splittings D_1-D_2 , D_2-C_8 , and C_9-C_8 plotted in Figs. A.4a to c. As was observed for the probe laser scans (Sect. 4.4), a significant scatter of results was found for these experiments. Figs. A.4d to f display the results of the same recordings, where the frequency offsets inferred from the wavemeter data were replaced with the laser frequency control voltage data in the horizontal axes of Fig. A.3. The scaling factor between frequency and voltage differences was evaluated as the average of the ratios of the theoretical fre-

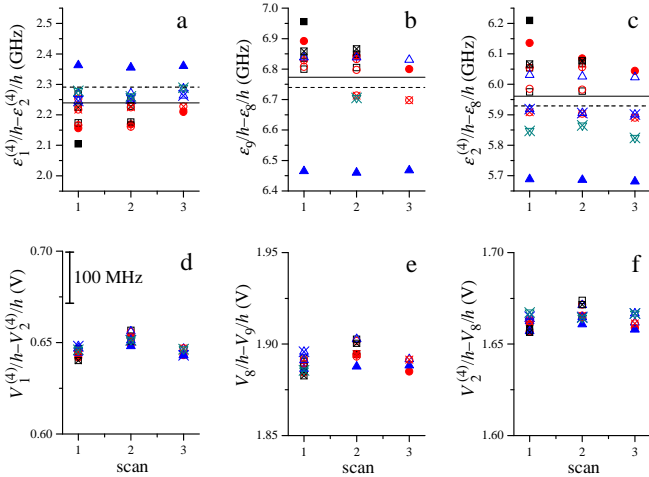


Figure A.4: Results of saturated absorption data yielding fit positions of the C_8 , D_2 , C_9 , and D_1 lines for series of 3 repeated scans (see Fig. A.3). Top (a to c): frequency splittings. Bottom (d to f): frequency control voltage differences. a,d: for the D_1 - D_2 interval. b,e: for the C_8 - C_9 interval. c,f: for the C_8 - D_2 interval. The solid and dashed lines in graphs a to c are the averaged data and computed values, respectively.

quency splittings (the dashed lines in Figs. A.4a to c) to the measured voltage splittings (in Figs. A.4d to f).

The scatter of the voltage splittings was significantly lower than that inferred from wavelength data, as appears on the statistical summary of the plotted results listed in Table A.1. A four- to eight-fold reduction of the standard

line names	data type	av.-th. (MHz)	SD (MHz)	SE (MHz)	N_s
$C_9 - C_8$	λ	33.7	135	28	23
$D_2 - C_8$	λ	31.9	131	24	29
$D_2 - D_1$	λ	-51.5	61	11	23
$C_9 - C_8$	V	-15.9	20.7	4.2	23
$D_2 - C_8$	V	-15.8	16.1	3	29
$D_2 - D_1$	V	11.7	15.5	2.9	23

Table A.1: Statistics for frequency splitting data compiled in Fig. A.4. Columns 3 to 5 contain the differences between the averages of the fit frequencies and the computed values, the standard deviation and the standard error of the fit frequencies. The first three lines are data from wavemeter readings, the last three lines from control voltage values (see text, data types λ or V). N_s is the number of scans used in the averages.

deviation of the three probed line splittings is evidenced, with a significant reduction of the differences from expected values (lines 4 to 6 vs. lines 1 to 3 in Table A.1).

The results of these series of recordings are thus affected by the measurement errors of the wavemeter in a way similar to those of Sect. 4.4. Moreover, since the pump diode

laser frequency is known to be reliably controlled by its temperature (therefore, by the control voltage in these experiments), the large reduction of errors in line splittings expressed as functions of this voltage further demonstrates that the frequency dependence of the wavemeter errors was the limiting factor for the precision of our Doppler-free measurement on the 706.5 nm transition.

References

- [1] T. Gentile, P.-J. Nacher, B. Saam, and T. Walker. ‘Optically polarized ^3He .’ *Rev. Mod. Phys.*, 89:045004 (2017).
- [2] A. Dantan, G. Reinaudi, A. Sinatra, F. Laloë, et al. ‘Long-lived quantum memory with nuclear atomic spins.’ *Phys. Rev. Lett.*, 95(12):123002 (2005).
- [3] Y. Zhan, X. Peng, S. Li, L. Zhang, et al. ‘Observation of transferred dressed spin effect via metastability-exchange collisions in He-3 atoms.’ *Appl. Phys. B*, 125(9):170 (2019).
- [4] S. Li, Y. Zhan, X. Peng, J. Chen, et al. ‘Linear and nonlinear coherence transfer of resonant nuclear-spin-dressed effect via metastability-exchange collisions.’ *J. Phys. B: At. Mol. Opt. Phys.*, 53(6):065202 (2020).
- [5] H. Gilles, J. Hamel, and B. Cheron. ‘Laser pumped He-4 magnetometer.’ *Rev. Sci. Instrum.*, 72(5):2253–2260 (2001).
- [6] F. Beato, E. Belorizky, E. Labyt, M. Le Prado, et al. ‘Theory of a ^4He parametric-resonance magnetometer based on atomic alignment.’ *Phys. Rev. A*, 98:053431 (2018).
- [7] G. Lieb, T. Jager, A. Palacios-Laloy, and H. Gilles. ‘All-optical isotropic scalar ^4He magnetometer based on atomic alignment.’ *Rev. Sci. Instrum.*, 90(7):075104 (2019).
- [8] M. Kodaira and T. Watanabe. ‘Collisional Transfer of Triplet Excitations between Helium Atoms.’ *J. Phys. Soc. Jpn.*, 27(5):1301–1309 (1969).
- [9] D. Vranceanu, S. Kotochigova, and H. Sadeghpour. ‘Pressure broadening and shift of He($2^3P_{0,1,2}$)-He(2^3S) lines.’ *Phys. Rev. A*, 69(2):022714 (2004).
- [10] L. Scheerer. ‘Collision-Induced Mixing in the 2^3P Levels of Helium.’ *Phys. Rev.*, 160(1):76–80 (1967).
- [11] A. Dia, P.-J. Nacher, M. Abboud, and G. Tastevin. ‘Spectroscopic study of collisions in the 2^3P state of ^3He and ^4He in low pressure gas discharges.’ In ‘25 ème congrès général de la Société Française de Physique,’ Nantes, France (2019).
- [12] M. Fred, F. Tomkins, J. Brody, and M. Hamermesh. ‘The Spectrum of ^3HeI .’ *Phys. Rev.*, 82(3):406–421 (1951).
- [13] J. Brochard, H. Chantrel, and P. Jacquinet. ‘Étude des niveaux de ^3He par spectroscopie optique à très basse température.’ *J. Phys. Radium*, 19(5):515–522 (1958).
- [14] J. Su and J. Nicol. ‘Measurements of self broadening of the triplet line λ 706.5 nm in helium.’ *J. Phys. B: At. Mol. Opt. Phys.*, 23(14):2215–2222 (1990).

- [15] J. Su and J. Nicol. ‘Pressure shift of the helium triplet line λ 706.5 nm.’ *J. Phys. B: At. Mol. Opt. Phys.*, 26(2):255–260 (1993).
- [16] M. Andersson and L. Pendrill. ‘Improved Measurements of the Hyperfine Structure of the $1s3s^3S_1$ State of He-3.’ *Phys. Scripta*, 30(6):403–406 (1984).
- [17] E. Courtade, F. Marion, P.-J. Nacher, G. Tastevin, et al. ‘Magnetic field effects on the 1083 nm atomic line of helium.’ *Eur. Phys. J. D*, 21(1):25–55 (2002).
- [18] D. Morton, Q. Wu, and G. Drake. ‘Energy levels for the stable isotopes of atomic helium (^4He I and ^3He I).’ *Can. J. Phys.*, 84(2):83–105 (2006).
- [19] Q. Wu. ‘Precision calculation of electronic g_J factors for n^3S_1 states of ^4He and $^7\text{Li}^+$ ion.’ *J. Phys. B: At. Mol. Opt. Phys.*, 39(20):4213–4219 (2006).
- [20] G. Drake, W. Nörtershäuser, and Z. C. Yan. ‘Isotope shifts and nuclear radius measurements for helium and lithium.’ *Can. J. Phys.*, 83(4):311–325 (2005).
- [21] R. Hilborn. ‘Einstein coefficients, cross-sections, f values, dipole-moments, and all that.’ *Am. J. Phys.*, 50(11):982–986 (1982).
- [22] M. Millard, P. Yaney, B. Ganguly, and C. DeJoseph. ‘Diode laser absorption measurements of metastable helium in glow discharges.’ *Plasma Sources Sci. Technol.*, 7(3):389–394 (1998).
- [23] R. Hilborn. ‘Einstein coefficients, cross sections, f values, dipole moments, and all that.’ ArXiv:physics/0202029.
- [24] A. Nikiel-Osuchowska, G. Collier, B. Glowacz, T. Palasz, et al. ‘Metastability exchange optical pumping of ^3He gas up to hundreds of millibars at 4.7 Tesla.’ *Eur. Phys. J. D*, 67(9):200 (2013).
- [25] M. Pinard, C. Aminoff, and F. Laloë. ‘Velocity-selective optical pumping and Doppler-free spectroscopy.’ *Phys. Rev. A*, 19(6):2366–2370 (1979).
- [26] W. Wiese and J. Fuhr. ‘Accurate Atomic Transition Probabilities for Hydrogen, Helium, and Lithium.’ *J. Phys. Chem. Ref. Data*, 38:565–719 (2009).
- [27] W. Demtröder. *Laser Spectroscopy*, volume 2, chapter 2, pages 83–147. Springer (2015). ISBN 978-3-662-44640-9. doi:10.1007/978-3-662-44641-6.
- [28] P.-J. Nacher and M. Leduc. ‘Optical pumping in ^3He with a laser.’ *J. Phys-Paris*, 46(12):2057–2073 (1985).
- [29] M. Batz, P.-J. Nacher, and G. Tastevin. ‘Fundamentals of metastability exchange optical pumping in helium.’ *J. Phys. Conf. Ser.*, 294(1):012002 (2011).
- [30] G. Tastevin and P.-J. Nacher. ‘NMR measurements of hyperpolarized He-3 gas diffusion in high porosity silica aerogels.’ *J. Chem. Phys.*, 123(6):064506 (2005).
- [31] P.-J. Nacher. ‘Magnetic-field Coils for Metastability-exchange Optical Pumping, Optical Spectroscopy, and Magnetic Resonance of Helium.’ (2021). Preprint, <https://hal.archives-ouvertes.fr/hal-03243760>.
- [32] A. Kramida, Yu. Ralchenko, J. Reader, and NIST ASD Team. NIST Atomic Spectra Database (ver. 5.8), [Online]. Available: <https://physics.nist.gov/asd> [2020, December 7]. National Institute of Standards and Technology, Gaithersburg, MD. (2020).
- [33] K. Koenig, P. Imgram, J. Kraemer, B. Maass, et al. ‘On the performance of wavelength meters: Part 2—frequency-comb based characterization for more accurate absolute wavelength determinations.’ *Appl. Phys. B*, 126(5):86 (2020).
- [34] N. Bigelow, P.-J. Nacher, and M. Leduc. ‘Accurate optical measurement of nuclear polarization in optically pumped ^3He gas.’ *J. Phys. II*, 2(12):2159–2179 (1992).
- [35] C. Talbot, M. Batz, P.-J. Nacher, and G. Tastevin. ‘An accurate optical technique for measuring the nuclear polarisation of ^3He gas.’ *J. Phys. Conf. Ser.*, 294:012008 (2011).
- [36] R. Whitley and C. Stroud. ‘Double optical resonance.’ *Phys. Rev. A*, 14(4):1498–1513 (1976).
- [37] C. Cohen-Tannoudji, J. Dupont-Roc, and G. Grynberg. *Atom-Photon Interactions: Basic Processes and Applications*. Wiley, New York (1992). ISBN 978-0-471-29336-1.
- [38] J. Mompert and R. Corbalan. ‘Generalized Einstein B coefficients for coherently driven three-level systems.’ *Phys. Rev. A*, 63(6):063810 (2001).
- [39] B. Aurand, S. Kuschel, C. Rödel, M. Heyer, et al. ‘Creating circularly polarized light with a phase-shifting mirror.’ *Opt. Express*, 19(18):17151–17157 (2011).
- [40] D. Bloch, G. Trenec, and M. Leduc. ‘Isotope shift of the 2^3S_1 - 2^3P transition in helium.’ *J. Phys. B: At. Mol. Opt. Phys.*, 18(6):1093–1100 (1985).
- [41] K. Saleh, J. Millo, A. Didier, Y. Kersalé, et al. ‘Frequency stability of a wavelength meter and applications to laser frequency stabilization.’ *Appl. Opt.*, 54(32):9446–9449 (2015).
- [42] L. Couturier, I. Nosske, F. Hu, C. Tan, et al. ‘Laser frequency stabilization using a commercial wavelength meter.’ *Rev. Sci. Instrum.*, 89(4):043103 (2018).